ATMOSPHERIC ENVIRONMENT: X 32 (2026) 100533

Contents lists available at ScienceDirect

Atmospheric Environment: X

journal homepage: www.journals.elsevier.com/atmospheric-environment-x

Variability of columnar greenhouse gases across atmospheric transport regimes over Thessaloniki, Greece using FTIR spectrometry

Thomas Panou [a,*], Marios Mermigkas [b], Chrysanthi Topaloglou [a], Dimitrios Balis [a], Carlos Alberti [c], Darko Dubravica [c], Frank Hase [c]

[a] Laboratory of Atmospheric Physics, School of Physics, Faculty of Natural Sciences, Aristotle University of Thessaloniki, Campus Box 149, Thessaloniki, 54124, Greece
[b] Institute for Astronomy, Astrophysics, Space Applications and Remote Sensing, National Observatory of Athens, GR-15236, Athens, Greece
[c] Institute of Meteorology and Climate Research (IMK-ASF), Karlsruhe Institute of Technology, Karlsruhe, Germany

ARTICLE INFO

Keywords:
Keywords Greenhouse gases
FTIR spectrometry
EM27/SUN
COCCON
HYSPLIT
Trajectory clustering
Air-mass transport

ABSTRACT

Understanding how atmospheric transport conditions are associated with greenhouse gas (GHG) variability is essential for interpreting columnar observations over urban environments. This study combines EM27/SUN measurements of XCO_2, XCH_4, and XCO over Thessaloniki, Greece, during 2019–2024 with seven-day HYbrid Single-Particle Lagrangian Integrated Trajectory (HYSPLIT) backward trajectories to investigate recurring air-mass transport regimes. Six dominant regimes were identified, representing Eastern Europe, Southwestern Europe, Northwestern Europe, North Europe, North America, and the Balkans. After removal of the estimated seasonal cycle and long-term trend, residual anomalies differed significantly among transport regimes for all three gases. XCH_4 showed the largest contrasts, with positive median anomalies for Eastern Europe and the Balkans and the lowest median for Southwestern Europe. XCO_2 showed smaller differences, with Eastern Europe characterized by a negative median residual, whereas XCO exhibited the highest positive median anomaly for Eastern Europe. Seasonal co-variability between gases also varied among regimes. Winter ΔXCO_2–ΔXCH_4 correlations were positive across all six regimes ($R = 0.65$–0.92), whereas summer relationships were predominantly negative. ΔXCO_2–ΔXCO showed its highest winter correlation for Northwestern Europe ($R = 0.70$), which also showed a negative summer relationship ($R = -0.44$). ΔXCH_4–ΔXCO remained positive across all regimes, with notable correlations for North America in winter ($R = 0.65$) and Eastern Europe in summer ($R = 0.72$). Sensitivity tests showed that the main geographical transport patterns and anomaly characteristics were generally preserved under alternative trajectory initialization times and arrival heights, highlighting the importance of season and air-mass history for interpreting long-term urban FTIR observations.

1. Introduction

Accurate observations of atmospheric greenhouse gases (GHGs) are essential for understanding the evolution of the Earth's climate system and for evaluating the effectiveness of mitigation strategies. According to the Sixth Assessment Report of the Intergovernmental Panel on Climate Change (IPCC), the sustained increase in atmospheric GHG concentrations since the mid-twentieth century has been the principal driver of observed climate change (Gulev et al., 2021). Continuous observations from both ground-based and satellite platforms provide complementary information for monitoring the atmospheric abundance and variability of key species such as CO_2, CH_4, and CO. At the same time, national and international climate policies increasingly require independent observational capabilities to support GHG emission assessments and verify reported emission reductions. In Europe, these needs have become even more prominent under the European Green Deal, which highlights the importance of reliable monitoring and verification frameworks for achieving climate neutrality. Consequently, there is growing interest in observational approaches that can improve the interpretation of atmospheric GHG variability while reducing uncertainties associated with emission estimates and atmospheric transport.

Atmospheric CO_2 has increased from approximately 278 ppm during the pre-industrial era to more than 422 ppm in 2024, primarily as a

* Corresponding author.
E-mail addresses: tpanou@physics.auth.gr (T. Panou), mmermigk@physics.auth.gr (M. Mermigkas), chtopal@auth.gr (C. Topaloglou), balis@auth.gr (D. Balis), carlos.alberti@kit.edu (C. Alberti), darko.dubravica@kit.edu (D. Dubravica), frank.hase@kit.edu (F. Hase).

https://doi.org/10.1016/j.aeaoa.2026.100533
Received 22 May 2026; Received in revised form 4 November 2026; Accepted 5 November 2026
Available online 6 November 2026
2590-1621/© 2026 The Authors. Published by Elsevier Ltd. This is an open access article under the CC BY license (http://creativecommons.org/licenses/by/4.0/).

consequence of human activities (Gulev et al., 2021; Lan et al., 2025a). Although land-use change contributed substantially during the early stages of industrialization, fossil-fuel combustion has become the dominant driver of the continuing increase in atmospheric CO_2 (Canadell et al., 2021; Friedlingstein et al., 2020). Part of these emissions is continuously removed by natural carbon sinks, with terrestrial ecosystems and the global ocean together absorbing roughly half of anthropogenic CO_2 emissions through biological and physicochemical processes (Gruber et al., 2023; Keenan and Williams, 2018).

Methane (CH_4) is the second most important anthropogenic GHG after carbon dioxide and has contributed approximately 0.6 °C to the observed global warming since pre-industrial times (Szopa et al., 2021). Despite its lower atmospheric abundance compared with CO_2, methane exerts a strong radiative effect and continues to increase globally because emissions exceed atmospheric removal (Ferretti et al., 2005). Its atmospheric lifetime is approximately nine years, with oxidation by hydroxyl (OH) radicals representing the dominant removal pathway (Myhre et al., 2013). Methane originates from a combination of anthropogenic and natural sources. Major anthropogenic emissions arise from fossil-fuel production, livestock farming, rice cultivation and waste management, whereas natural emissions are dominated by wetlands (Canadell et al., 2021; Ciais et al., 2014; Jacob et al., 2022).

Although carbon monoxide (CO) is not a greenhouse gas, it plays a central role in atmospheric chemistry by regulating the oxidizing capacity of the troposphere. Carbon monoxide is emitted primarily from incomplete combustion associated with transportation, residential heating, industrial activities, biomass burning, and other combustion-related processes (Zhong et al., 2017). It reacts efficiently with hydroxyl (OH) radicals, thereby reducing the availability of the primary atmospheric oxidant and indirectly extending the lifetime of methane while also contributing to tropospheric ozone formation (Daniel and Solomon, 1998; Jacob, 1999; Lelieveld et al., 2016; Wuebbles and Hayhoe, 2002). Because CO and CO_2 are frequently co-emitted during combustion, atmospheric CO observations are often used as an indicator of combustion-related emission sources, particularly in urban environments (MacDonald et al., 2023; Silva et al., 2013). Despite an overall decline in global atmospheric CO concentrations during recent decades, largely attributed to reductions in anthropogenic emissions, substantial spatial and temporal variability persists owing to biomass burning, atmospheric transport, and changes in chemical production (Deeter et al., 2017; Gaubert et al., 2017; Jiang et al., 2017; Zheng et al., 2019). Given its relatively short atmospheric lifetime of approximately one to three months, CO is particularly sensitive to recent emission sources and atmospheric transport, making it a valuable tracer for investigating regional and long-range transport processes (Seinfeld and Pandis, 2016).

The different atmospheric lifetimes and source distributions of CO_2, CH_4, and CO contribute significantly to the variability observed at a measurement site. Air-mass history can therefore provide useful context for interpreting the observed columnar variability in relation to nearby emissions, regional inflow, and long-range transport.

Ground-based Fourier transform spectrometers have become an important component of the global GHG observing system, providing highly accurate columnar measurements that complement satellite observations. The Total Carbon Column Observing Network (TCCON), established in 2004, comprises high-resolution Fourier transform spectrometers that retrieve accurate and precise column-averaged dry-air mole fractions of atmospheric trace gases from direct solar absorption spectra in the near-infrared spectral region (Wunch et al., 2011). Complementary to TCCON, the COllaborative Carbon Column Observing Network (COCCON), established in 2014, utilizes the Bruker EM27/SUN portable FTIR instrument (Frey et al., 2019; Herkommer et al., 2024; Sha et al., 2020). Compared with high-resolution TCCON instrumentation, the EM27/SUN provides a compact solution that facilitates continuous observations of CO_2, CH_4, CO, and H_2O. Its portability and relatively low operating cost have enabled its widespread use in urban, regional, and campaign-based GHG monitoring studies (Makarova et al., 2021; Tu et al., 2022; Vogel et al., 2019). Previous investigations have employed EM27/SUN instruments and the COCCON network to characterize urban GHG variability, assess regional emission signatures, validate satellite observations, and support atmospheric transport studies in diverse environments (Frausto-Vicencio et al., 2023; Frey et al., 2021; Humpage et al., 2024; Sha et al., 2025).

The HYbrid Single-Particle Lagrangian Integrated Trajectory (HYSPLIT) model is widely used to identify atmospheric transport pathways, and clustering multiple trajectories enables recurring air-mass regimes to be identified and compared with variations in trace gases, aerosols, and regional pollution levels (Draxler and Hess, 1998; Stein et al., 2015). Regional applications in Greece have applied air-mass trajectory analysis to examine background pollution and the influence of wildfires on atmospheric composition (Masoom et al., 2023; Rizos et al., 2022). However, the systematic combination of multi-year trajectory clustering with urban column-averaged GHG observations remains limited, particularly in the Eastern Mediterranean.

Since 2019, continuous GHG observations using the Bruker EM27/SUN instrument have been performed in Thessaloniki, Greece in the framework of COCCON (Mermigkas et al., 2021), providing total columnar concentrations of CO_2, CH_4, H_2O and CO in an urban environment. Thessaloniki, the second-largest city of Greece, is a major metropolitan center in the northern part of the country and is classified as an urban site. It is directly influenced by a variety of anthropogenic emission sources, including traffic, residential heating, industrial zones, landfills, and nearby agricultural activities, and is occasionally affected by biomass burning events (Koukouli et al., 2025; Michailidis et al., 2024). Thessaloniki is located in the Eastern Mediterranean, a region characterized by complex atmospheric circulation patterns where air masses originating from continental Europe, the Balkans, the Mediterranean basin, and occasionally North Africa interact. In addition, the region lies near areas with different levels of economic development and emission characteristics across southeastern Europe. As a result, the region is particularly sensitive to both local emissions and the influence of long-range transport on GHG concentrations. The COCCON station located in the city center of Thessaloniki, Greece (40.63° N, 22.95° E, 67 m AMSL), is strategically positioned to observe columnar variability influenced by urban, regional, and large-scale transport conditions.

Building on previous urban applications of EM27/SUN observations, this study systematically links six years (2019–2024) of column-averaged XCO_2, XCH_4, and XCO measurements with cluster-labelled atmospheric transport regimes over Thessaloniki. The novelty of this work lies in combining a multi-year analysis of atmospheric transport regimes with deseasonalized and detrended residual anomalies at an urban site in the Eastern Mediterranean. Specifically, we (i) characterize the climatology and seasonal distribution of the dominant transport regimes, (ii) evaluate differences in the observed concentrations and columnar anomalies among the identified transport regimes, and (iii) examine the seasonal co-variability of ΔXCO_2, ΔXCH_4 and ΔXCO within each transport regime. These analyses are intended to identify associations between atmospheric transport conditions and columnar variability rather than to provide quantitative source attribution.

2. Materials and methods

2.1. Materials

2.1.1. Bruker EM27/SUN measurements

For the purposes of this study, a six-year dataset (2019–2024) of solar absorption measurements acquired with the Bruker EM27/SUN Fourier Transform Infrared (FTIR) spectrometer in Thessaloniki, Greece (Mermigkas et al., 2025) was used. EM27/SUN spectrometers operated within the COCCON network follow common calibration and validation procedures and are deployed at several sites worldwide. Developed collaboratively by the Karlsruhe Institute of Technology (KIT) and Bruker Optics, the EM27/SUN is built to capture direct solar spectra

(Frey et al., 2019). Details on the instrument design and operation can be found in earlier studies (Alberti et al., 2022; Gisi et al., 2012; Hase et al., 2016). Each EM27/SUN spectrometer is calibrated against a common reference instrument collocated with the Karlsruhe TCCON station, ensuring network-wide consistency and traceability of the retrieved GHG columns to the TCCON reference scale and, ultimately, the WMO calibration scale (Alberti et al., 2022; Frey et al., 2019; Herkommer et al., 2024). The instrument's raw interferograms were processed using the standard PROFFASTpylot (v2.4) processing chain (Feld et al., 2024). The processing includes automated quality-control procedures during the preprocessing stage, where interferograms are screened for quality and corrected for source brightness fluctuations (SBF) caused by clouds or short-term variations in solar irradiance, thereby improving the stability of the retrieved spectra. Following the spectral retrieval, air-mass-dependent corrections are applied to reduce systematic biases associated with solar zenith angle (SZA) (Frey et al., 2019; Herkommer et al., 2024; Sha et al., 2020). The total column dry-air mole fraction, denoted as X_{gas}, is calculated as:

$$X_{gas} = \frac{TC_{gas}}{TC_{O_2}} \times 0.2095 \quad (1)$$

where TC_{gas} is the retrieved total column of the target gas, TC_{O_2} is the retrieved oxygen column, and the multiplicative factor (0.2095) represents the assumed mole fraction of oxygen in dry air.

In this study, the short-term precision was evaluated from the deviations of individual XCO_2, XCH_4, and XCO measurements from a 20 min rolling mean. The resulting precisions for the Thessaloniki EM27/SUN were 0.104 ppm for XCO_2, 0.557 ppb for XCH_4 and 0.566 ppb for XCO, in good agreement with the expected performance of EM27/SUN spectrometers reported by Frey et al. (2019) and Hase et al. (2016).

2.1.2. The HYbrid Single-Particle Lagrangian Integrated Trajectory (HYSPLIT) model

Back trajectory analysis is commonly used to identify the transport history of air masses arriving at an observational site, and to identify dominant upwind flow pathways. In this study, three-dimensional kinematic backward trajectories were computed using the HYSPLIT model (version 5.3) to characterize the atmospheric transport regimes affecting the Thessaloniki FTIR station (Draxler and Hess, 1998). Trajectories were generated once per day at 12:00 UTC to provide a consistent daily descriptor of the dominant synoptic-scale transport conditions influencing the measurement site, covering a 168-h (seven-day) period for the entire 2019–2024 dataset (Rizos et al., 2022).

The Bruker EM27/SUN instrument performs direct-sun columnar measurements and therefore operates only during daylight conditions. At the Thessaloniki site, most observations are acquired between approximately 08:00 and 12:00 UTC. A trajectory arrival time of 12:00 UTC was therefore selected as representative of the measurement period contributing to the daily mean columnar observations. This choice is also physically justified because midday conditions are generally characterized by a well-developed atmospheric boundary layer, resulting in enhanced vertical mixing and more spatially representative air masses (Stull, 1988). The objective of the trajectory analysis is to characterize the dominant transport regime associated with each measurement day rather than to analyze sub-daily transport variability. The seven-day temporal window was selected to capture both regional and long-range transport patterns and to identify broad transport regimes and residence regions associated with variability in the observed columnar GHG concentrations (Cheng and Kabela, 2016).

An arrival height of 1500 m above mean sea level (AMSL), approximately corresponding to the 850 hPa level, was selected for the reference trajectory calculations (Pérez-Ramírez et al., 2012; Toledano et al., 2009). This height provides a representation of lower-tropospheric transport while limiting the influence of near-surface local circulation (Seibert et al., 2000; Stull, 1988). Analysis of the European Centre for Medium-Range Weather Forecasts (ECMWF) Reanalysis version 5 (ERA5) hourly data on single levels for boundary layer height over the broader Central Macedonia region during the 2019–2024 period yielded seasonal mean values of approximately 600 m during winter and 1400 m during summer, whereas the climatological mean for the complete dataset was approximately 1000 ± 500 m (Hersbach et al., 2020). The fixed 1500 m arrival height does not represent the same position relative to the boundary layer throughout the year but instead serves as a consistent reference level for characterizing the dominant lower-tropospheric transport regime associated with each measurement day.

To assess the sensitivity of the trajectory classification to these two initialization parameters, two complementary tests were performed. First, trajectories initialized at 10:00 and 12:00 UTC at 1500 m AMSL were compared to examine whether the selected arrival time affected the geographical transport patterns. Second, the trajectory analysis was repeated at 500 m AMSL using the reference arrival time of 12:00 UTC to evaluate the effect of a substantially lower arrival height. The time sensitivity test produced only minor changes in the geographical structure of the trajectories, while the lower arrival height mainly resulted in differences in trajectory altitude. The resulting trajectory clusters and associated GHG anomaly statistics were also evaluated under both alternative configurations. The sensitivity results are presented in Section 3.1 including the geographical comparison shown in Fig. 1.

Meteorological input fields were taken from the Global Data Assimilation System (GDAS) produced by the National Centers for Environmental Prediction (NCEP) at 1° × 1° resolution. These datasets are routinely pre-processed by NOAA's Air Resources Laboratory into a standardized format compatible with HYSPLIT, ensuring consistent meteorological input for all trajectory calculations (Cheng and Kabela, 2016).

2.2. Methods

2.2.1. Trajectory cluster analysis

The extracted seven-day trajectories were grouped using the hierarchical agglomerative clustering scheme included in HYSPLIT, which clusters trajectories based on their spatial similarity. The clustering metric is derived from the spatial variance of each cluster, quantified through the Total Spatial Variance (TSV), which provides a measure of within cluster homogeneity and between cluster separation (Stein et al., 2015).

During the iterative merging process, the clustering algorithm progressively combines trajectories that minimize the increase in TSV. To determine the optimal number of clusters, the percentage change in TSV was evaluated at each merging step. Reducing the number of clusters from six to five resulted in an increase in TSV, indicating that solutions with fewer than six clusters lead to a substantial loss of cluster separation and merging of distinct transport regimes. Solutions with a higher number of clusters primarily resulted in subdivisions of already similar trajectory groups, producing comparable transport patterns but with increased fragmentation into smaller subsets. This behavior is reflected in the relatively similar TSV values obtained for cluster numbers greater than six (e.g., seven or eight clusters). Such subdivision does not provide additional physical insight and reduces the statistical robustness of the cluster-based analysis, particularly when linking transport regimes with observed GHG variability.

The resulting classification yielded six distinct trajectory clusters that represent the dominant transport regimes affecting the study site during the 2019–2024 period. These clusters summarize the variability in both regional and long-range air-mass regimes and provide a structured basis for linking transport history with observed GHG variability.

It should be noted that back trajectories are inherently subject to increasing uncertainty with transport time, particularly for multi-day simulations. Previous studies have shown that trajectory position

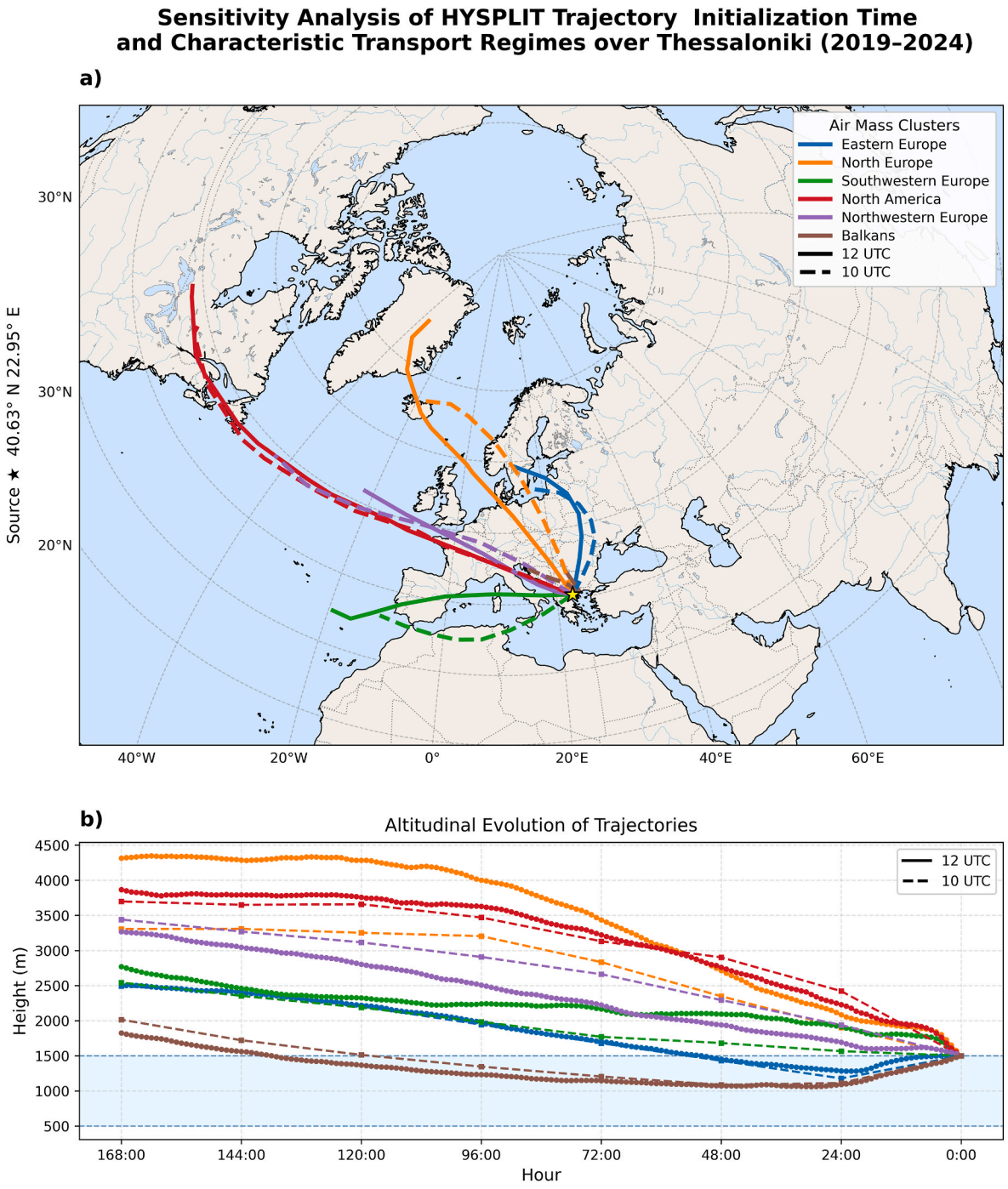


Fig. 1. Sensitivity analysis of HYSPLIT trajectory initialization time and characteristic transport regimes over Thessaloniki during 2019–2024. (a) Comparison of the centroid seven-day backward trajectories initialized at 10:00 UTC (dashed lines) and 12:00 UTC (solid lines) for the six trajectory clusters, color-coded by transport regime. (b) Corresponding altitudinal evolution of the centroid trajectories. The shaded blue region denotes the climatological boundary layer height derived from ERA5 (1000 ± 500 m), averaged over the domain covering Thessaloniki and the surrounding Central Macedonia region.

errors may reach approximately 15–30% of the travel distance, while mean position errors after 72 h transport can exceed 400 km (Stein et al., 2015; Stohl, 1998). In addition, Radenz et al. (2021) suggested that a first-order estimate of the uncertainty for a single air-parcel location is on the order of ~20% of the distance from the trajectory origin. Therefore, the resulting clusters should be interpreted as representative and indicative of dominant flow regimes and their variability, rather than precise or unique representations of air-mass origin.

2.2.2. Statistical analysis of EM27/SUN observations based on air mass trajectory clusters

To examine the relationship between atmospheric transport regimes and observed GHG variability, HYSPLIT trajectory clusters were integrated into a structured analysis framework. The analysis evaluates whether different transport regimes are associated with systematic differences in the distributions of XCO_2, XCH_4, and XCO across seasons, focusing on how atmospheric transport conditions are associated with variability in the EM27/SUN columnar observations rather than on specific source attribution. Daily averaged EM27/SUN observations

were first grouped according to their corresponding trajectory clusters. The seasonal distribution of the clusters was also examined to characterize changes in the frequency of the different transport regimes throughout the year. This classification provided time series spanning multiple years and labelled by cluster, allowing comparison of concentration and anomaly distributions among transport regimes. To reduce the residual variability associated with the transport regimes, each gas time series was first deseasonalized and then detrended. A multi-year mean annual cycle (MAC) was derived from monthly averages, which helped accommodate gaps in the observational record, and was subsequently interpolated using a continuous fit. Specific gas preprocessing was applied where episodic variability could substantially influence the estimation of the seasonal cycle. For XCO, summer days (June–August) with values exceeding 100 ppb were excluded from the calculation of the MAC to reduce the influence of episodic enhancements. This threshold was derived from summertime observations in 2019, 2020, and 2022, for which the mean XCO was approximately 89 ppb with a standard deviation of approximately 5 ppb, placing the 100 ppb threshold approximately two standard deviations above the mean ($+2\sigma$). For XCH_4, the seasonal cycle was constructed using the initial part of the dataset (2019–2020), which showed more stable temporal behavior, thereby reducing the influence of interannual variability and anomalous periods on the estimated seasonal cycle. The deseasonalized time series for each gas was then obtained as:

$$X_{deseasonalized} = X_{daily} - X_{MAC} \quad (2)$$

where X_{daily} represents the daily averaged column-averaged dry-air mole fraction and X_{MAC} corresponds to the multi-year mean annual cycle.

A linear trend was next fitted to the deseasonalized series and removed, yielding the final anomalies:

$$\Delta X = X_{deseasonalized} - X_{trend} \quad (3)$$

where X_{trend} represents the long-term linear trend component estimated from a least-squares linear regression applied to the deseasonalized time series.

The resulting anomalies (ΔX) represent residual variability after removal of the estimated seasonal cycle and long-term trend and were analyzed for each cluster using time series, seasonal stratification, and box summaries. In addition to the anomaly analysis, seasonal relationships between the gases were examined. Pairwise relationships between ΔXCO_2–ΔXCH_4, ΔXCO_2–ΔXCO, and ΔXCH_4–ΔXCO were examined for each cluster and separately for winter and summer.

The sensitivity of the anomaly statistics to the trajectory configurations described in Section 2.1.2 was assessed across gases and transport regimes. Median values from the reference configuration (1500 m, 12:00 UTC) were compared with those obtained using trajectories initialized at 1500 m at 10:00 UTC and at 500 m at 12:00 UTC. The shift in the median was quantified relative to the variability of the corresponding reference distribution using Eq. (4), where ΔMedian represents the difference between the reference and sensitivity medians, and the interquartile range (IQR) is defined as $Q_{75} - Q_{25}$.

$$S = \frac{|\Delta \text{Median}|}{\text{IQR}} = \frac{|\text{Median}_{ref} - \text{Median}_{sen}|}{Q_{75} - Q_{25}} \quad (4)$$

An uncertainty propagation framework was implemented to quantify the confidence of the derived anomalies (ΔX values). Two main sources of uncertainty were considered: (i) the uncertainty associated with the estimation of the seasonal cycle (deseasonalization), and (ii) the uncertainty introduced by the linear trend fitting and removal. Assuming these components are independent, the total uncertainty of the anomaly time series was calculated as the root-sum-square (RSS) of the individual contributions. The resulting total uncertainties are ± 1.73 ppm for XCO_2, ± 6.54 ppb for XCH_4, and ± 1.93 ppb for XCO.

2.2.3. Statistical assessment of residual anomalies and Co-variability analysis

Statistical analyses were performed on the daily residual anomalies obtained after removal of the mean seasonal cycle and long-term trend. For the comparison of residual distributions among the six trajectory clusters, a non-parametric Kruskal–Wallis test was applied separately for each gas, with $p < 0.05$ indicating significant differences among the cluster distributions. In addition, uncertainty in the median residual anomaly of each gas and cluster was quantified using percentile bootstrap resampling with 10,000 iterations to derive 95% confidence intervals. Whether these intervals included zero was used descriptively to assess whether the median residual anomaly of each cluster remained consistently positive or negative. For the gas co-variability analysis, all available paired daily residual observations were considered separately for each gas pair, season and trajectory cluster. Pearson's correlation coefficient (R) and its two-sided nominal p-value were calculated, and ordinary least-squares linear regression was used to quantify the linear relationship between paired residuals. Paired bootstrap resampling with 10,000 iterations was used to derive 95% confidence intervals for both R and the regression slope, while preserving the pairing between gas observations. To account for multiple testing, the nominal p-values from all 36 correlation tests (three gas pairs $\times$ two seasons $\times$ six trajectory clusters) were jointly adjusted using the Benjamini–Hochberg false discovery rate (BH-FDR) procedure. Correlations with $q < 0.05$ were considered statistically supported. To assess the sensitivity of the correlation results to temporal dependence among consecutive observations, an additional thinning-based robustness test was performed. Consecutive daily observations were removed so that retained observations were separated by at least two calendar days. The 36 correlation tests were then repeated, and the corresponding p-values were again adjusted using the BH-FDR procedure.

3. Results and discussion

3.1. Characteristic transport regimes

The present section focuses on the characteristics of the transport regimes summarized by the centroid trajectories (Fig. 1a). Sensitivity tests were performed to examine the effect of trajectory initialization time and arrival height on the resulting transport classification. Changing the initialization time from 12:00 to 10:00 UTC had a limited effect on the overall geographical transport patterns and cluster structure. The largest differences occurred for the northern transport regimes (North Europe and Northwestern Europe), with a mean horizontal separation of approximately 800 km and a mean vertical difference of about 600 m for the North Europe trajectories. Such differences are expected for long-range transport regimes, since trajectory uncertainty increases with backward integration time and progressively amplifies small differences in the initial conditions. Despite these differences, the main geographical transport sectors and the overall cluster structure remained broadly consistent between the two initialization times. Reducing the arrival height from 1500 to 500 m AMSL resulted in trajectories that generally evolved at lower altitudes and were therefore more frequently located within or closer to the boundary layer, while the main geographical transport patterns represented by the six clusters were generally preserved.

The 12:00 UTC centroid provides a simplified representation of the dominant flow patterns within each cluster, while the corresponding vertical profiles (Fig. 1b) describe the evolution of air-mass altitude over the seven-day transport period. The Eastern Europe and Balkan clusters are characterized by relatively short transport pathways, slower air-mass movement, and predominantly lower altitudes throughout most of their trajectory. The Southwestern Europe and Northwestern Europe clusters show intermediate continental transport, with trajectories spanning both lower and mid-tropospheric altitudes. In contrast, the North America and North Europe clusters are characterized by long-

range trajectories that extend over considerably greater distances and remain at higher altitudes during a substantial part of the seven-day period. These trajectories typically descend from altitudes above 3000 m before approaching the lower troposphere closer to the measurement site. The six clusters represent distinct combinations of transport direction, travel distance, and vertical evolution, providing the basis for examining their seasonal occurrence and their association with the observed columnar variability in the following sections.

3.2. Seasonal distribution of air mass clusters

The 168-h backward trajectories were grouped by season to examine how the occurrence of the transport regimes influencing Thessaloniki varies throughout the year. Fig. 2 illustrates the seasonal frequency of occurrence of trajectory clusters for winter (December–February), spring (March–May), summer (June–August) and autumn (September–November). The seasonal distributions reveal marked seasonal contrasts between regional and long-range transport regimes.

During summer, air masses associated with the Eastern Europe and Balkan transport regimes dominate the transport statistics, which together account for more than half of all summertime cases. These clusters represent short-range circulation patterns typical of stagnant and thermally driven meteorology over southeastern Europe. In contrast, winter is characterized by contributions from North America and North Europe, reflecting enhanced influence of synoptic-scale westerly and high-latitude flow. Spring and autumn show a more mixed distribution, combining both regional clusters (e.g., Balkans, Eastern Europe) and intercontinental origins. These seasonal differences characterize transport conditions associated with GHG variability and provide context for interpreting the patterns observed across the different transport regimes in the subsequent sections.

3.3. Variability of observed XCO_2, XCH_4, and XCO across transport regimes

3.3.1. Time series of GHGs grouped by transport regimes

Fig. 3a–c presents the daily mean XCH_4 (Fig. 3a), XCO_2 (Fig. 3b), and XCO (Fig. 3c) time series for 2019–2024, color-coded according to the associated trajectory cluster. The daily mean columnar observations reflect variability associated with background atmospheric conditions, atmospheric transport, and other processes (e.g., long-term trends, seasonal biospheric and chemical cycles, regional emissions, boundary-layer dynamics, and meteorological variability). The anomaly analysis presented in Section 3.3.3 reduces the influence of the seasonal cycle and long-term trend, allowing the residual variability to be compared among the different transport regimes. Previous studies at the Thessaloniki FTIR station suggest that XCO_2 seasonal changes are mainly driven by the balance between biospheric uptake and anthropogenic emissions (Mermigkas et al., 2021). XCH_4 is influenced by regional biogenic and anthropogenic sources, while its atmospheric lifetime and seasonal evolution are largely controlled by oxidation with OH radicals, its dominant atmospheric sink. Similarly, XCO variability reflects emissions from combustion processes and chemical removal through reactions with OH (Lelieveld et al., 2016). Mermigkas et al. (2025) showed that the diurnal and short-term variability of XCO_2, XCH_4, and XCO at the Thessaloniki FTIR station varied with season and was modulated by wind speed and direction, with concurrent enhancements occurring during summer and autumn under southwesterly local winds of low to moderate intensity. They also found strong co-variability between ΔXCH_4 and ΔXCO throughout the year, consistent with common sources and sinks, and linked simultaneous enhancements in summer 2021 to the regional transport of wildfire emissions from southern Greece.

Within this broader framework, the trajectory clusters are used to examine how the observed concentrations vary under different air-mass histories rather than to provide source attribution. The Balkans and Eastern Europe clusters account for a large fraction of the observations and show relatively high concentrations and pronounced day-to-day variability across the three gases. The North America and North Europe clusters generally show lower concentrations and less day-to-day variability, while the Southwestern and Northwestern Europe clusters exhibit intermediate behavior. These differences provide an initial indication that the observed columnar variability is not distributed uniformly among the identified transport regimes. Beyond these contrasts in atmospheric transport, the time series spanning multiple years also reveal distinct long-term trends and seasonal behavior. Both XCO_2 and XCH_4 exhibit a persistent increase over the study period, consistent with global observations. XCO_2 shows a comparatively smooth and gradual evolution, reflecting its well-mixed atmospheric nature. In contrast, XCH_4 displays more pronounced intra-annual variability, which varies with regional transport conditions and interannual atmospheric variability. Carbon monoxide exhibits a weaker long-term increase than XCO_2 and XCH_4, while retaining pronounced short-term and summertime variability, particularly during periods associated with

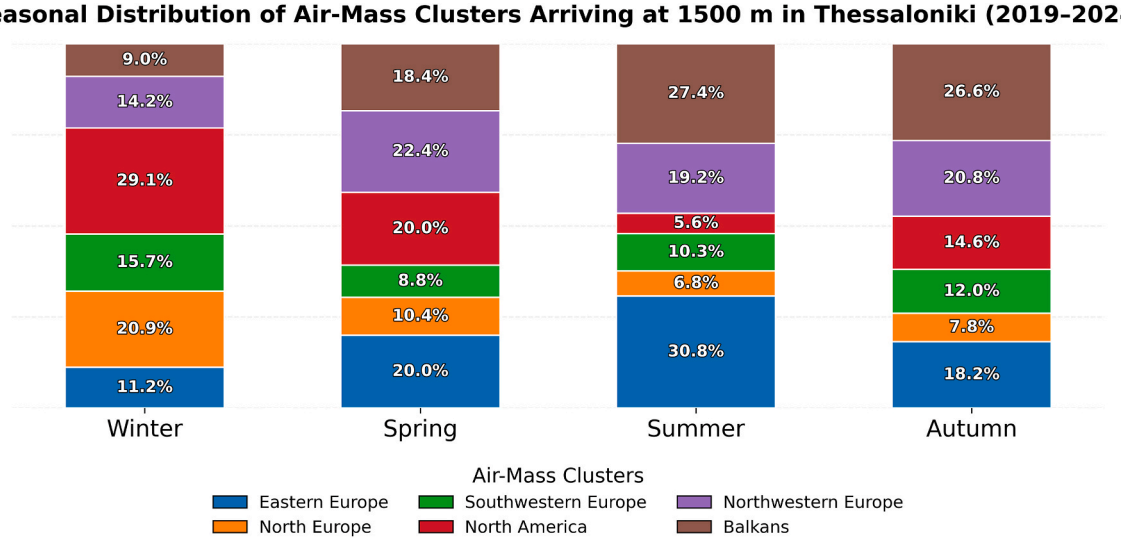


Fig. 2. Seasonal distribution (%) of air-mass transport regimes arriving at Thessaloniki, based on 168-h backward trajectories computed with the HYSPLIT model. Each bar represents a season (winter, spring, summer, autumn), with colors indicating the relative contribution of each transport cluster.

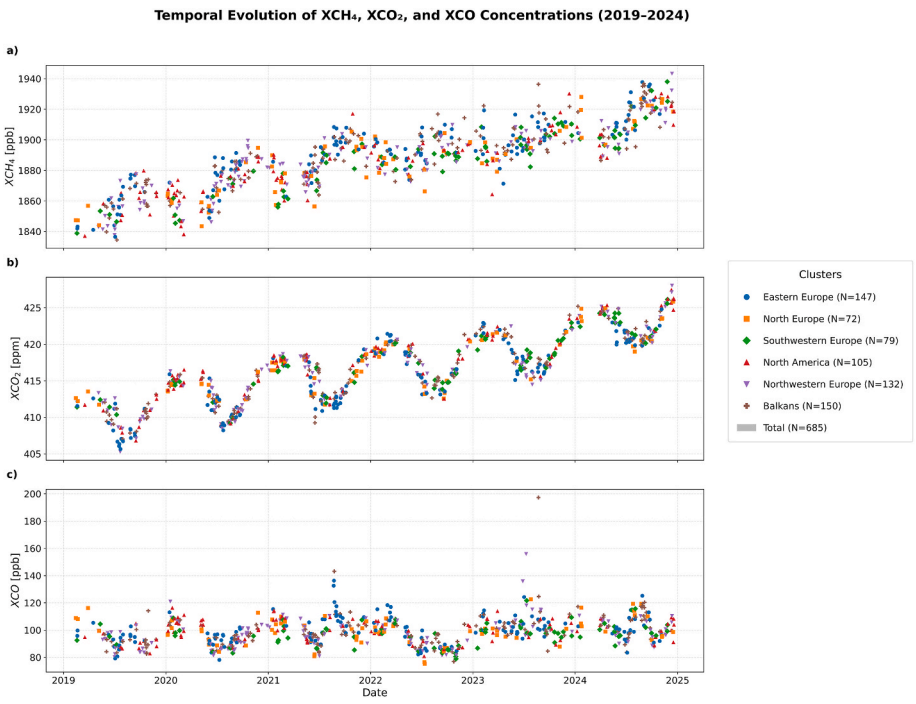


Fig. 3. Cluster-labelled daily time series of column-averaged dry-air mole fractions measured by the EM27/SUN spectrometer in Thessaloniki during 2019–2024. (a) XCH_4 (ppb), (b) XCO_2 (ppm), and (c) XCO (ppb). Data points are color-coded according to the transport regime assigned to each day.

regional fire activity and emissions from combustion processes.

These qualitative features are consistent with the quantitative metrics summarized in Table 1. XCO_2 exhibits relatively low intra-annual variability (2.30 ± 0.20 ppm) and a mean value of 416.64 ± 4.56 ppm, together with a positive trend (2.26 ± 0.06 ppm yr^{-1}). Methane shows higher variability (12.14 ± 1.60 ppb) and a mean concentration of 1888.26 ± 21.56 ppb, along with a comparable increasing trend (11.20 ± 0.25 ppb yr^{-1}). In contrast, XCO is characterized by substantial variability (7.92 ± 0.98 ppb), while exhibiting a weaker trend (1.56 ± 0.24 ppb yr^{-1}) compared with the other gases. Although the absolute increase in CO is smaller relative to the other species, its pronounced intra-annual variability highlights its sensitivity to short-lived episodic enhancements, including periods affected by regional fire activity. The stronger short-term variability of XCH_4 and XCO is also evident in the daily time series, where both gases show more pronounced fluctuations than XCO_2.

3.3.2. *Spatial distribution of anthropogenic GHG emissions*

The spatial distribution of anthropogenic CO_2 and CH_4 emissions from the Emissions Database for Global Atmospheric Research (EDGAR) provides additional geographic context for the identified transport regimes (Fig. 4a and b) (Crippa et al., 2025). The EDGAR database, developed by the Joint Research Centre (JRC) of the European Commission in collaboration with the International Energy Agency (IEA), provides global gridded anthropogenic emissions from major sectors including energy production, industrial processes, transportation, buildings, fuel exploitation, agriculture, and waste management. The data used here have a spatial resolution of 0.1° × 0.1°. The emission fields are used as a qualitative spatial reference for the regions crossed by the HYSPLIT trajectories, providing geographical context without attributing the observed column concentrations to specific source regions or sectors.

The Eastern Europe and Balkan trajectories cross regions with comparatively high anthropogenic emissions (e.g., residential heating, fossil-fuel use, livestock agriculture, and waste-management activities) in the EDGAR inventory, particularly for CH_4. This spatial overlap provides geographical context for interpreting the observed columnar variability but does not establish that emissions from these regions contributed to the observed anomalies over Thessaloniki.

The Northwestern Europe and Southwestern Europe trajectories also intersect regions with moderate and high anthropogenic emissions in the EDGAR inventory. The North America and North Europe regimes include substantially longer transport pathways and likewise cross areas with anthropogenic CO_2 and CH_4 emissions. Overall, the EDGAR emission maps provide complementary spatial context for the transport regimes identified by the HYSPLIT analysis. They are therefore considered alongside, rather than used to explain, the differences in GHG anomalies examined in Section 3.3.3.

3.3.3. *Transport regime differences in ΔX variability*

The cluster-labelled time series presented in Section 3.3.1 show substantial temporal variability in all three gases, including their seasonal cycles and multi-year trends. The XCO_2, XCH_4, and XCO time series were therefore deseasonalized and detrended following the methodology described in Section 2.2.2 before comparing the transport regimes. The resulting residual anomalies (ΔX) represent the variability remaining after removal of the estimated seasonal cycle and long-term trend. Although this procedure reduces the influence of these temporal components, the residual anomalies may still reflect meteorological, chemical, biospheric, and emission-related variability. The cluster-based analysis therefore examines how the remaining columnar variability is associated with different air-mass histories, without independently

Table 1
Summary of multi-year statistical characteristics of XCO_2, XCH_4, and XCO (2019–2024), including maximum, minimum and mean values, as well as intra-annual variability. All metrics are based on daily mean values. Intra-annual variability is defined as the standard deviation of daily mean concentrations within each year, averaged over the study period.

	XCO_2 (ppm)	XCO (ppb)	XCH_4 (ppb)
Max values	428.02 ± 0.14	119.26 ± 2.63	1943.25 ± 1.21
Min values	405.27 ± 0.61	75.30 ± 1.24	1834.49 ± 1.07
Mean values	416.64 ± 4.56	98.06 ± 8.82	1888.26 ± 21.56
Intra-annual variability	2.30 ± 0.20	7.92 ± 0.98	12.14 ± 1.60

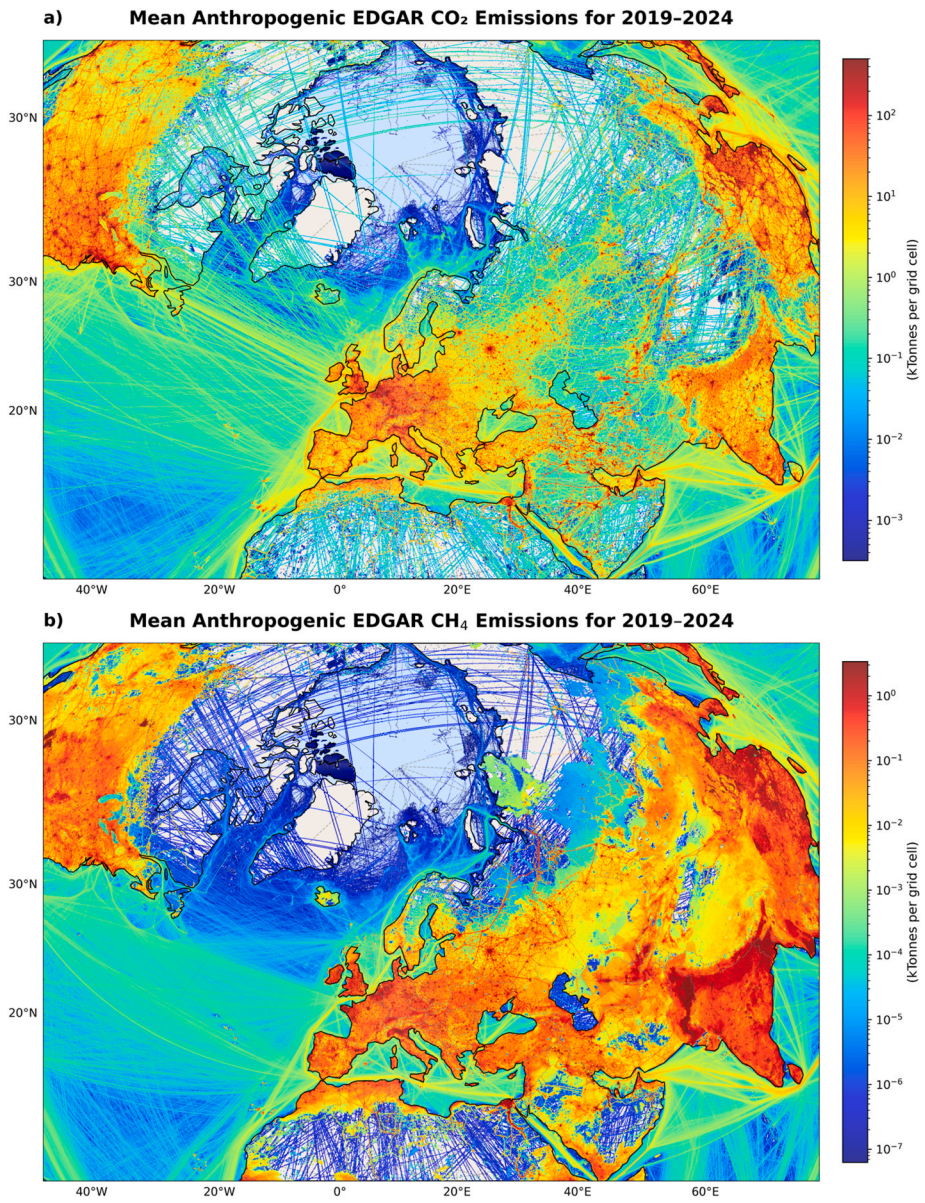


Fig. 4. Mean anthropogenic carbon dioxide (a) and methane (b) emissions derived from the EDGAR database, for the period 2019–2024 (Crippa et al., 2025). The maps represent the average total anthropogenic emissions from all source sectors.

quantifying the contributions of these processes. Fig. 5 shows their distributions across the six trajectory clusters for the full 2019–2024 period, while Fig. 6 focuses on selected years. For XCH_4 and XCO_2, the years 2021 and 2024 were selected, respectively, as they correspond to documented global growth anomalies of these gases, whereas for XCO each cluster is represented by the year with its highest annual median ΔXCO. Differences among the six cluster distributions were assessed using the Kruskal–Wallis test. The 95% bootstrap confidence interval of the median was additionally used to describe the uncertainty in the central anomaly of each cluster.

Methane shows the most pronounced differences among transport regimes over the full 2019–2024 period. The overall comparison indicates significant differences among the six cluster distributions (Kruskal–Wallis $H = 31.34$, $p < 0.001$; Fig. 5a). Eastern Europe and the Balkans show positive median anomalies, whereas the remaining clusters are centered below zero, with Southwestern Europe exhibiting the most negative median ΔXCH_4. In 2021, elevated ΔXCH_4 values occurred across several clusters, while no significant differences were detected among their distributions ($H = 9.14$, $p = 0.104$; Fig. 6a). This reduced contrast among transport regimes may reflect the widespread increase in atmospheric methane observed during that year. Previous studies have associated this global increase with changes in atmospheric chemistry and enhanced emissions from natural sources, particularly wetlands (Ciais et al., 2026; Lan et al., 2025b). These broader atmospheric changes may therefore represent one of the factors contributing to the elevated XCH_4 anomalies observed over Thessaloniki in 2021, although their specific contribution cannot be determined from the present analysis.

Carbon dioxide anomalies show smaller differences among the transport regimes than methane, although the six cluster distributions still differ significantly over the full 2019–2024 period ($H = 12.53$, $p = 0.028$; Fig. 5b), with median ΔXCO_2 values remaining relatively close to zero across the clusters. The Eastern Europe cluster is characterized by a negative median anomaly, indicating association with air masses relatively depleted in CO_2 compared with the residual background over Thessaloniki. In 2024, positive median anomalies occur across several transport regimes, while the differences among the cluster distributions are marginally significant ($H = 11.43$, $p = 0.044$; Fig. 6b).

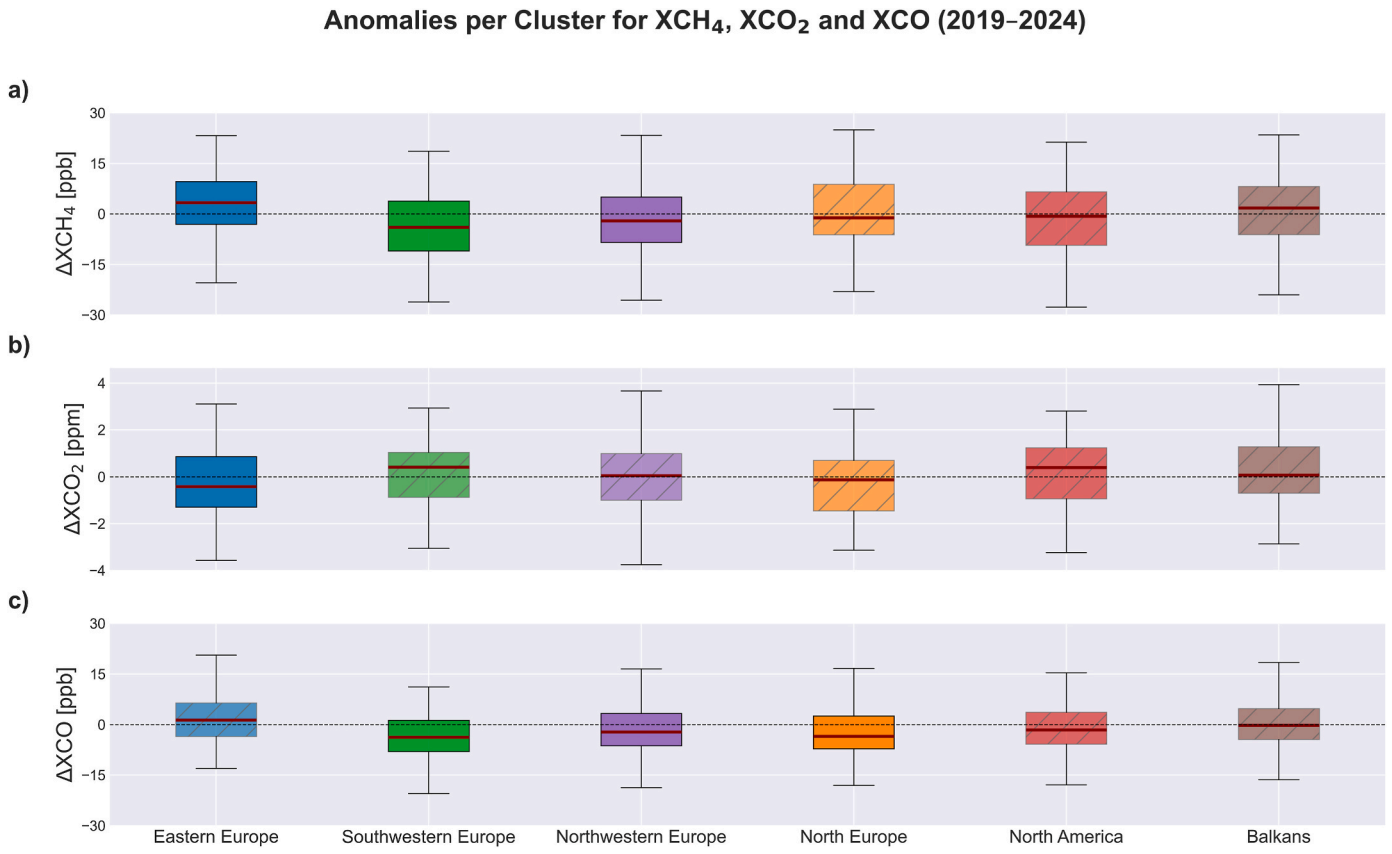


Fig. 5. Cluster-labelled daily residual anomalies (ΔX) for methane (XCH_4) (a), carbon dioxide (XCO_2) (b), and carbon monoxide (XCO) (c) for the period 2019–2024. Boxes represent the interquartile range (25th–75th percentiles), with the median shown as a horizontal line. Whiskers extend beyond the interquartile range according to the standard boxplot convention. Hatched boxes indicate clusters for which the 95% bootstrap confidence interval of the median includes zero, while non-hatched boxes indicate clusters for which the confidence interval does not include zero. The horizontal dashed line represents zero residual anomaly.

The widespread positive ΔXCO_2 values coincide with reports of an exceptionally large increase in global atmospheric CO_2 during the same year (Dong et al., 2026; Friedlingstein et al., 2025; Lan et al., 2025b).

Carbon monoxide also varies among the transport regimes over the full 2019–2024 period, with significant differences among the six cluster distributions ($H = 29.49$, $p < 0.001$; Fig. 5c). Eastern Europe shows the highest positive median anomaly, whereas the distributions of the other clusters are generally centered closer to or below zero. XCO also exhibits intermittent positive excursions, consistent with the episodic variability observed in the daily time series. This behavior is further illustrated in Fig. 6c, in which each cluster is represented by the year with the highest annual median ΔXCO. Because each cluster in Fig. 6c is represented by a different year, differences between boxes combine year and cluster effects and should not be compared across clusters. For this reason, no Kruskal–Wallis test was applied to this panel. All selected years (2021, 2023 and 2024) coincide with periods of documented wildfire activity in Greece and the wider Balkan region (Koukouli et al., 2025; Masoom et al., 2023; Mermigkas et al., 2025; Michailidis et al., 2024; Sedano et al., 2025). In addition, the year selected for the North America regime (2021) coincides with an exceptionally intense North American fire season, during which the satellite-derived burned area across the United States and Canada was the highest of the 2002–2021 record (Jain et al., 2024). These events provide relevant context for the elevated XCO anomalies, although their contribution to the anomalies observed under individual transport regimes cannot be determined from the present analysis.

The main cluster-based anomaly patterns were generally preserved across the alternative trajectory configurations examined in Section 2.1.2. Most changes in median anomalies were small relative to the interquartile range of the corresponding reference distributions. Across both sensitivity configurations, the S value (Eq. (4)) ranged from 0.01 to 0.34 for XCH_4, from 0.01 to 0.20 for XCO_2, and from 0.00 to 0.42 for XCO. The most noticeable sensitivity to arrival height was found for XCH_4 in the North Europe cluster, where lowering the trajectory arrival height from 1500 to 500 m shifted the median from −1.15 to +4.02 ppb ($S = 0.34$). This pattern may partly reflect the slight spatial displacement between the corresponding trajectory pathways, together with the lower-altitude evolution of the 500 m trajectories, which may expose the sampled air masses to a different combination of near-surface and regional emission influences. XCO showed comparatively greater sensitivity in the North America cluster for the 500 m configuration, where the median shifted from −1.60 to −5.54 ppb ($S = 0.42$). In this case, the lower arrival height may similarly alter the relative contribution of air masses encountered along the transport pathway, potentially reducing the influence of elevated transported air. XCO_2 showed comparatively smaller changes, with S values remaining between 0.01 and 0.20 across all clusters and configurations. Overall, these results suggest that the main anomaly patterns are largely preserved across trajectory configurations, although some long-range transport regimes exhibit greater sensitivity to the selected initialization parameters.

3.4. Seasonal relationships between ΔXCO_2, ΔXCH_4, and ΔXCO

While Section 3.3.3 highlights how the residual anomalies of each gas differ among transport regimes, the relationships among the gases provide additional insight into the underlying atmospheric variability. Examining the correlations between variations in ΔXCO_2, ΔXCH_4, and ΔXCO allows assessment of the extent to which these gases correlate consistently under common transport and seasonal conditions. Pairwise relationships between ΔXCO_2–ΔXCH_4 (Fig. 7), ΔXCO_2–ΔXCO (Table 2),

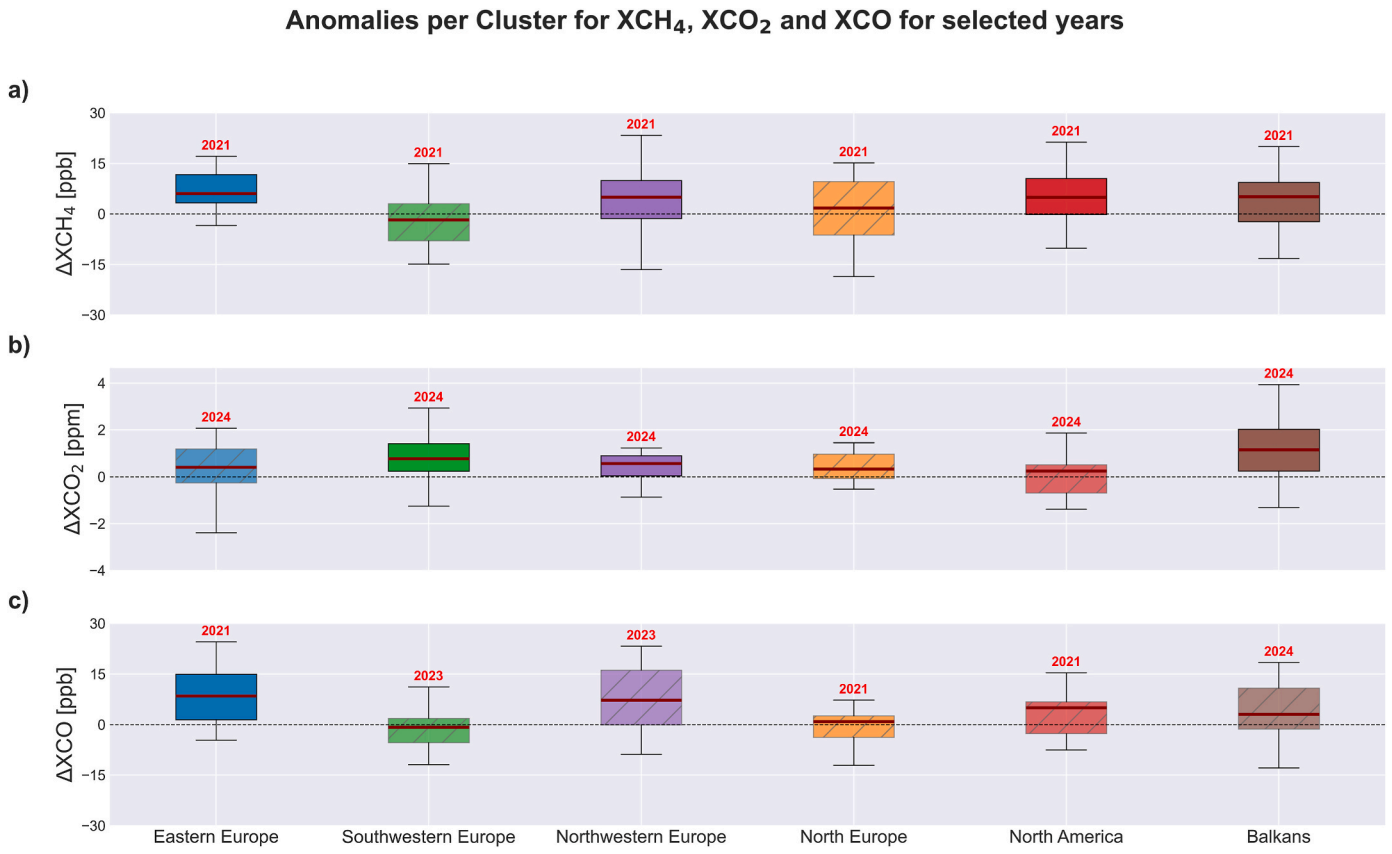


Fig. 6. Cluster-labelled daily ΔX anomalies for methane (XCH_4) (a), carbon dioxide (XCO_2) (b), and carbon monoxide (XCO) (c) for selected years over the period 2019–2024. For XCH_4 and XCO_2, boxplots correspond to data from 2021 and 2024, respectively, the years of the documented global growth anomalies of these gases. Panel c (XCO) is illustrative: each cluster is represented by the year with its highest annual median ΔXCO, indicated above each box, and the clusters are therefore not directly comparable. The boxplot format and statistical representation follow those described in Fig. 5.

and ΔXCH_4–ΔXCO (Table 2) were examined separately for winter and summer conditions and for each trajectory cluster. Pearson correlation coefficients were calculated from daily paired residual observations. To account for multiple comparisons, the resulting p-values were adjusted across the 36 tests using the BH-FDR procedure, with $q < 0.05$ used as the criterion for statistical support.

The largest seasonal contrast is observed for the ΔXCO_2–ΔXCH_4 relationship (Fig. 7). During winter, positive correlations occur across all six transport regimes ($R = 0.65$–0.92), and all six relationships meet the $q < 0.05$ criterion. This indicates that positive co-variability is a common winter feature across transport regimes rather than a pattern confined to a specific air mass pathway. The highest correlations are observed for Northwestern Europe and the Balkans ($R = 0.92$ and 0.90). Summer shows a distinctly different pattern. Correlations are predominantly negative, but statistical support is retained only for Southwestern Europe, Northwestern Europe, and the Balkans. Southwestern and Northwestern Europe both show correlations of $R = -0.53$, while the Balkans show $R = -0.41$. This shift from consistently positive winter correlations to weaker or negative summer relationships indicates a pronounced seasonal change in the co-variability of XCO_2 and XCH_4. One possible contribution is the year-to-year variability in biospheric CO_2 uptake during summer, which can alter XCO_2 independently of the processes affecting XCH_4 (Friedlingstein et al., 2025; Sepúlveda et al., 2014).

The ΔXCO_2–ΔXCO relationship shows a less uniform seasonal pattern across the transport regimes (Table 2). Winter correlations are positive for all six clusters, ranging from $R = 0.41$ to 0.70, with statistically supported relationships for North Europe, North America, and Northwestern Europe. The strongest correlation occurs for Northwestern Europe ($R = 0.70$), followed by North America ($R = 0.61$). During summer, both the direction and magnitude of the relationships vary among transport regimes. Northwestern Europe is the only cluster retaining statistical support, with a negative correlation ($R = -0.44$). This seasonal contrast may partly reflect the reduced contribution of wintertime combustion-related activity during summer, together with seasonal changes in atmospheric mixing and boundary-layer conditions.

For ΔXCH_4–ΔXCO, positive correlations occur across all transport regimes in both winter and summer (Table 2). During summer, statistical support is limited to Eastern Europe and the Balkans, with correlations of $R = 0.72$ and $R = 0.35$, respectively. Winter correlations are also consistently positive, with the strongest relationships observed for North America ($R = 0.65$) and Northwestern Europe ($R = 0.62$). The strength and statistical support of this positive co-variability therefore vary with season and transport regime. This behaviour may be consistent with periods in which CH_4 and CO are affected by common or concurrent atmospheric influences, although the correlations alone cannot identify the processes or sources responsible for their co-variability (Seinfeld and Pandis, 2016; Szopa et al., 2021). The main co-variability patterns were generally preserved after temporal thinning. The correlation sign remained unchanged in 35 of the 36 comparisons, and the principal relationships remained statistically supported after correction for multiple testing. However, some secondary relationships, such as the winter ΔXCO_2–ΔXCO correlation for North Europe, no longer met the FDR criterion after thinning. Overall, these results suggest that the principal co-variability patterns were not solely driven by consecutive daily observations.

4. Conclusions

The combined use of long-term ground-based FTIR measurements

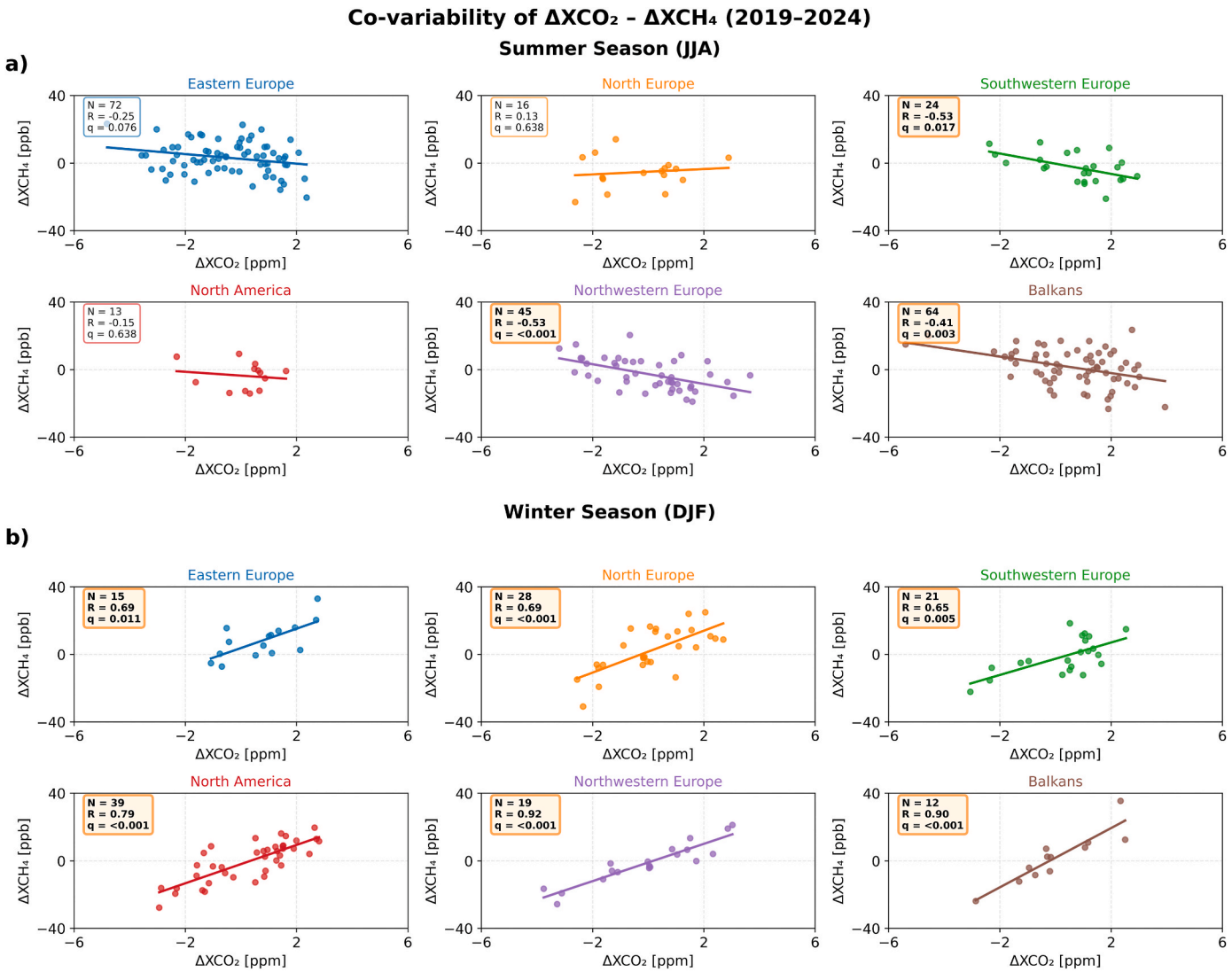


Fig. 7. Scatterplots of the relationship between ΔXCO_2 and ΔXCH_4 for each air-mass cluster during (a) summer (JJA) and (b) winter (DJF). Points represent paired daily residual anomalies, and solid lines show the corresponding ordinary least-squares linear fits. Each inset reports the number of paired daily observations (*N*), the Pearson correlation coefficient (*R*), and the Benjamini–Hochberg-adjusted *q* value. Orange-framed insets indicate statistically supported correlations ($q < 0.05$).

Table 2
Pearson correlation coefficients (R) for the seasonal ΔXCO_2–ΔXCO and ΔXCH_4–ΔXCO relationships across the six transport regimes. Values in bold indicate statistically supported correlations based on the Benjamini–Hochberg adjusted criterion ($q < 0.05$).

Air mass clusters	CO_2-CO (DJF)	CO_2-CO (JJA)	CH_4-CO (DJF)	CH_4-CO (JJA)
Eastern Europe	0.50	0.10	0.41	**0.72**
North Europe	**0.52**	0.38	0.24	0.47
Southwestern Europe	0.41	−0.27	0.26	0.34
North America	**0.61**	0.50	**0.65**	0.19
Northwestern Europe	**0.70**	**−0.44**	**0.62**	0.30
Balkans	0.56	0.22	0.45	**0.35**

and trajectory analysis provides a framework for examining associations between columnar variability and recurring atmospheric transport regimes while accounting for broader temporal variability. This approach offers useful context for interpreting long-term GHG observations in the Eastern Mediterranean. Six recurring transport regimes were identified, spanning regional pathways from Eastern Europe and the Balkans to long-range transport from northern, western, and transatlantic sectors. After removal of the estimated seasonal cycle and long-term trend, the residual anomalies revealed distinct responses among the three gases. XCH_4 showed the largest contrasts among transport regimes over 2019–2024, with positive median anomalies for Eastern Europe and the Balkans and negative medians for the remaining clusters. Southwestern Europe was particularly notable for its negative XCH_4 residuals, showing the lowest median anomaly among the identified regimes. XCO_2 exhibited smaller differences overall, with median anomalies generally remaining close to zero, although Eastern Europe was characterized by a negative median residual, while 2024 showed positive anomalies across several transport regimes. XCO exhibited greater episodic variability, with Eastern Europe showing the highest positive median anomaly over the full study period. These results indicate that the variability remaining after removal of the dominant temporal components is not distributed uniformly among the identified air mass histories. Sensitivity tests further showed that the main geographical transport patterns and cluster-level anomaly characteristics were generally maintained when the trajectory initialization time and arrival height were varied. Most changes in median anomalies were small relative to the variability of the corresponding reference distributions. Greater sensitivity was confined to specific long-range regimes, particularly XCH_4 for North Europe when

the arrival height was reduced to 500 m and XCO for North America. XCO_2 was comparatively insensitive to the alternative trajectory configurations, with relatively low S values ($S \leq 0.20$). The relationships among the residual gases also varied strongly with season and transport regime. Seasonal contrast was observed for ΔXCO_2–ΔXCH_4, with positive winter correlations across all six transport regimes that remained statistically supported after correction for multiple testing. In summer, the relationships were predominantly negative, with statistically supported correlations for Southwestern Europe, Northwestern Europe, and the Balkans. ΔXCO_2–ΔXCO showed a less uniform pattern across transport regimes, with Northwestern Europe exhibiting a notable seasonal contrast, characterized by a positive correlation in winter and a negative one in summer. ΔXCH_4–ΔXCO remained positively correlated across the transport regimes in both seasons, with particularly notable relationships for North America in winter and Eastern Europe in summer. Together, these results indicate that the co-variability of the column-averaged gas concentrations varies with season and air-mass history rather than following a uniform relationship throughout the year. The co-variability patterns were also generally preserved after temporal thinning, suggesting that these relationships were not solely driven by consecutive daily observations. Despite these consistent patterns, several limitations should be considered when interpreting the results. The trajectory clusters should be interpreted as indicators of recurring large-scale air-mass histories rather than as vertically resolved representations of the atmospheric column sampled by the EM27/SUN. A single trajectory arrival height cannot reproduce the full vertical sensitivity of a columnar measurement. Furthermore, the quantitative separation of local and transported contributions is beyond the scope of the present analysis, as the observed anomalies and correlations cannot by themselves distinguish local influences from transported signals or identify individual emission sources. Future work aimed at more quantitative attribution would require complementary meteorological information, temporally resolved emission inventories, source-specific tracers, and higher-resolution atmospheric transport modelling. Within these limitations, the results show that incorporating air-mass history provides important context for interpreting long-term columnar observations of GHGs and related tracers in the Eastern Mediterranean.

CRediT authorship contribution statement

Thomas Panou: Writing – original draft, Visualization, Methodology, Investigation, Data curation, Conceptualization, Formal analysis. **Marios Mermigkas:** Methodology, Formal analysis, Data curation, Writing – review & editing, Validation. **Chrysanthi Topaloglou:** Writing – original draft, Visualization, Methodology, Investigation, Formal analysis, Conceptualization. **Dimitrios Balis:** Writing – review & editing, Supervision, Project administration, Methodology, Funding acquisition, Conceptualization. **Carlos Alberti:** Software, Formal analysis, Data curation, Methodology, Validation. **Darko Dubravica:** Software, Methodology, Formal analysis, Data curation, Writing – review & editing. **Frank Hase:** Supervision, Methodology, Investigation, Conceptualization, Writing – review & editing.

Funding

This study was supported by the project "Support for enhancing the operation of the National Network for Climate Change (CLIMPACT)", funded by the National Development Program and implemented by the General Secretariat for Research and Innovation (GSRI) (Project No. 2023NA11900001 – N. 5201588).

Declaration of competing interest

The authors declare that they have no known competing financial interests or personal relationships that could have appeared to influence the work reported in this paper.

Acknowledgments

We wholeheartedly acknowledge the support provided by the Karlsruhe Institute of Technology (KIT – "The Research University in the Helmholtz Association"). The authors would like to acknowledge the support provided by the AUTh IT Center throughout the progress of this research work. Results presented in this work have been produced using the Aristotle University of Thessaloniki (AUTh) High Performance Computing Infrastructure and Resources.

Data availability

The EM27/SUN FTIR spectrometer data over Thessaloniki, Greece, are available upon reasonable request from the corresponding author. Meteorological data used for the HYSPLIT simulations were obtained from the Global Data Assimilation System (GDAS) produced by the National Centers for Environmental Prediction (NCEP) and archived by NOAA's Air Resources Laboratory (NOAA ARL) and were downloaded via FTP from the NCEP/NOAA data archive (ftp://ftpprd.ncep.noaa.gov//pub/data/nccf/com/hysplit/prod/). Boundary layer height data were obtained from the European Centre for Medium-Range Weather Forecasts (ECMWF) Reanalysis version 5 (ERA5) hourly data on single levels, available through the Copernicus Climate Change Service (C3S) Climate Data Store (CDS).

References

Alberti, C., Hase, F., Frey, M., Dubravica, D., Blumenstock, T., Dehn, A., Castracane, P., Surawicz, G., Harig, R., Baier, B.C., Bès, C., Bi, J., Boesch, H., Butz, A., Cai, Z., Chen, J., Crowell, S.M., Deutscher, N.M., Ene, D., Franklin, J.E., García, O., Griffith, D., Grouiez, B., Grutter, M., Hamdouni, A., Houweling, S., Humpage, N., Jacobs, N., Jeong, S., Joly, L., Jones, N.B., Jouglet, D., Kivi, R., Kleinschek, R., Lopez, M., Medeiros, D.J., Morino, I., Mostafavipak, N., Müller, A., Ohyama, H., Palmer, P.I., Pathakoti, M., Pollard, D.F., Raffalski, U., Ramonet, M., Ramsay, R., Sha, M.K., Shiomi, K., Simpson, W., Stremme, W., Sun, Y., Tanimoto, H., Té, Y., Tsidu, G.M., Velazco, V.A., Vogel, F., Watanabe, M., Wei, C., Wunch, D., Yamasoe, M., Zhang, L., Orphal, J., 2022. Improved calibration procedures for the EM27/SUN spectrometers of the COllaborative Carbon Column Observing Network (COCCON). Atmos. Meas. Tech. 15, 2433–2463. https://doi.org/10.5194/AMT-15-2433-2022.

Canadell, J.G., Monteiro, P.M.S., Costa, M.H., Cunha, L.C. da, Cox, P.M., Eliseev, A.V., Henson, S., Ishii, M., Jaccard, S., Koven, C., Lohila, A., Patra, P.K., Piao, S., Rogelj, J., Syampungani, S., Zaehle, S., Zickfeld, K., 2021. Global carbon and other biogeochemical cycles and feedbacks. In: Masson-Delmotte, V., Zhai, P., Pirani, A., Connors, S.L., Péan, C., Berger, S., Caud, N., Chen, Y., Goldfarb, L., Gomis, M.I., Huang, M., Leitzell, K., Lonnoy, E., Matthews, J.B.R., Maycock, T.K., Waterfield, T., Yelekçi, O., Yu, R., Zhou, B. (Eds.), Climate Change 2021: the Physical Science Basis. Contribution of Working Group I to the Sixth Assessment Report of the Intergovernmental Panel on Climate Change. Cambridge University Press, Cambridge, UK, pp. 673–816. https://doi.org/10.1017/9781009157896.007.

Cheng, M.-D., Kabela, E.D., 2016. Effects of downscaled high-resolution meteorological data on the PSCF identification of emission sources. Atmos. Environ. 137, 146–154. https://doi.org/10.1016/j.atmosenv.2016.04.043.

Ciais, P., Sabine, C., Bala, G., Bopp, L., Brovkin, V., House, J.I., et al., 2014. Carbon and other biogeochemical cycles. In: Climate Change 2013: the Physical Science Basis. Contribution of Working Group I to the Fifth Assessment Report of the Intergovernmental Panel on Climate Change. Cambridge University Press, pp. 465–570. https://doi.org/10.1017/CBO9781107415324.015.

Ciais, P., Zhu, Y., Cai, Y., Lan, X., Michel, S., Zheng, B., Zhao, Y., Hauglustaine, D., Lin, X., Zhang, Y., et al., 2026. Why methane surged in the atmosphere during the early 2020s. Science 391, eadx8262. https://doi.org/10.1126/science.adx8262.

Crippa, M., Guizzardi, D., Pagani, F., Banja, M., Muntean, M., et al., 2025. GHG Emissions of all World Countries – 2025 Report (No. JRC143227). Publications Office of the European Union, Luxembourg. https://doi.org/10.2760/9816914.

Daniel, J.S., Solomon, S., 1998. On the climate forcing of carbon monoxide. J. Geophys. Res. Atmos. 103, 13249–13260. https://doi.org/10.1029/98JD00822.

Deeter, M.N., Edwards, D.P., Francis, G.L., Gille, J.C., Martínez-Alonso, S., Worden, H. M., Sweeney, C., 2017. A climate-scale satellite record for carbon monoxide: the MOPITT version 7 product. Atmos. Meas. Tech. 10, 2533–2555. https://doi.org/10.5194/amt-10-2533-2017.

Dong, G., Jiang, F., Ju, W., Peñuelas, J., Ciais, P., Zhang, Yongguang, Xiao, J., Wang, X., Yuan, W., Huang, Y., Yue, C., Liu, L., Li, X., Fan, L., van der Werf, G.R., Wu, M., Wang, J., Zhou, Y., Tian, J., Wang, H., He, W., Zhang, L., Lv, G., Zhang, Yuanyuan, Chen, J.M., 2026. Dramatic increase in ecosystem respiration causes record-breaking

atmospheric CO_2 growth rate in 2024. Nat. Commun. 17, 5436. https://doi.org/10.1038/s41467-026-72189-y.
Draxler, R.R., Hess, G.D., 1998. An overview of the HYSPLIT_4 modelling system for trajectories. Aust. Meteorol. Mag. 47, 295–308.
Feld, L., Herkommer, B., Vestner, J., Dubravica, D., Alberti, C., Hase, F., 2024. PROFFASTpylot: Running PROFFAST with Python. J. Open Source Softw. 9, 6481. https://doi.org/10.21105/joss.06481.
Ferretti, D., Miller, J., White, J., Etheridge, D., Lassey, K., Lowe, D., Meure, C.M., Dreier, M., Trudinger, C., Van Ommen, T., et al., 2005. Unexpected changes to the global methane budget over the past 2000 years. Science 309, 1714–1717. https://doi.org/10.1126/science.1115193.
Frausto-Vicencio, I., Heerah, S., Meyer, A.G., Parker, H.A., Dubey, M., Hopkins, F.M., 2023. Ground solar absorption observations of total column CO, CO_2, CH_4, and aerosol optical depth from California's Sequoia Lightning Complex Fire: emission factors and modified combustion efficiency at regional scales. Atmos. Chem. Phys. 23, 4521–4543. https://doi.org/10.5194/acp-23-4521-2023.
Frey, M., Sha, M.K., Hase, F., Kiel, M., Blumenstock, T., Harig, R., Surawicz, G., Deutscher, N.M., Shiomi, K., Franklin, J.E., Bösch, H., Chen, J., Grutter, M., Ohyama, H., Sun, Y., Butz, A., Tsidu, G.M., Ene, D., Wunch, D., Cao, Z., Garcia, O., Ramonet, M., Vogel, F., Orphal, J., 2019. Building the COllaborative Carbon Column Observing Network (COCCON): long-term stability and ensemble performance of the EM27/SUN Fourier transform spectrometer. Atmos. Meas. Tech. 12, 1513–1530. https://doi.org/10.5194/AMT-12-1513-2019.
Frey, M.M., Hase, F., Blumenstock, T., Dubravica, D., Groß, J., Göttsche, F., Handjaba, M., Amadhila, P., Mushi, R., Morino, I., Shiomi, K., Sha, M.K., De Mazière, M., Pollard, D.F., 2021. Long-term column-averaged greenhouse gas observations using a COCCON spectrometer at the high-surface-albedo site in Gobabeb, Namibia. Atmos. Meas. Tech. 14, 5887–5911. https://doi.org/10.5194/amt-14-5887-2021.
Friedlingstein, P., O'Sullivan, M., Jones, M.W., Andrew, R.M., Hauck, J., Landschützer, P., Le Quéré, C., Li, H., Luijkx, I.T., Olsen, A., Peters, G.P., Peters, W., Pongratz, J., Schwingshackl, C., Sitch, S., Canadell, J.G., Ciais, P., Jackson, R.B., Alin, S.R., Arneth, A., Arora, V., Bates, N.R., Becker, M., Bellouin, N., Berghoff, C.F., Bittig, H.C., Bopp, L., Cadule, P., Campbell, K., Chamberlain, M.A., Chandra, N., Chevallier, F., Chini, L.P., Colligan, T., Decayeux, J., Djeutchouang, L.M., Dou, X., Duran Rojas, C., Enyo, K., Evans, W., Fay, A.R., Feely, R.A., Ford, D.J., Foster, A., Gasser, T., Gehlen, M., Gkritzalis, T., Grassi, G., Gregor, L., Gruber, N., Gürses, Ö., Harris, I., Hefner, M., Heinke, J., Hurtt, G.C., Iida, Y., Ilyina, T., Jacobson, A.R., Jain, A.K., Jarníková, T., Jersild, A., Jiang, F., Jin, Z., Kato, E., Keeling, R.F., Klein Goldewijk, K., Knauer, J., Korsbakken, J.I., Lan, X., Lauvset, S.K., Lefèvre, N., Liu, Z., Liu, J., Ma, L., Maksyutov, S., Marland, G., Mayot, N., McGuire, P.C., Metzl, N., Monacci, N.M., Morgan, E.J., Nakaoka, S.-I., Neill, C., Niwa, Y., Nützel, T., Olivier, L., Ono, T., Palmer, P.I., Pierrot, D., Qin, Z., Resplandy, L., Roobaert, A., Rosan, T.M., Rödenbeck, C., Schwinger, J., Smallman, T.L., Smith, S.M., Sospedra-Alfonso, R., Steinhoff, T., Sun, Q., Sutton, A.J., Séférian, R., Takao, S., Tatebe, H., Tian, H., Tilbrook, B., Torres, O., Tourigny, E., Tsujino, H., Tubiello, F., van der Werf, G., Wanninkhof, R., Wang, X., Yang, D., Yang, X., Yu, Z., Yuan, W., Yue, X., Zaehle, S., Zeng, N., Zeng, J., 2025. Global carbon budget 2024. Earth Syst. Sci. Data 17, 965–1039. https://doi.org/10.5194/essd-17-965-2025.
Friedlingstein, P., O'Sullivan, M., Jones, M.W., Andrew, R.M., Hauck, J., Olsen, A., Peters, G.P., Peters, W., Pongratz, J., Sitch, S., Quéré, C.L., Canadell, J.G., Ciais, P., Jackson, R.B., Alin, S., Aragão, L.E.O.C., Arneth, A., Arora, V., Bates, N.R., Becker, M., Benoit-Cattin, A., Bittig, H.C., Bopp, L., Bultan, S., Chandra, N., Chevallier, F., Chini, L.P., Evans, W., Florentie, L., Forster, P.M., Gasser, T., Gehlen, M., Gilfillan, D., Gkritzalis, T., Gregor, L., Gruber, N., Harris, I., Hartung, K., Haverd, V., Houghton, R.A., Ilyina, T., Jain, A.K., Joetzjer, E., Kadono, K., Kato, E., Kitidis, V., Korsbakken, J.I., Landschützer, P., Lefèvre, N., Lenton, A., Lienert, S., Liu, Z., Lombardozzi, D., Marland, G., Metzl, N., Munro, D.R., Nabel, J.E.M.S., Nakaoka, S.I., Niwa, Y., O'Brien, K., Ono, T., Palmer, P.I., Pierrot, D., Poulter, B., Resplandy, L., Robertson, E., Rödenbeck, C., Schwinger, J., Séférian, R., Skjelvan, I., Smith, A.J.P., Sutton, A.J., Tanhua, T., Tans, P.P., Tian, H., Tilbrook, B., Werf, G.V. D., Vuichard, N., Walker, A.P., Wanninkhof, R., Watson, A.J., Willis, D., Wiltshire, A. J., Yuan, W., Yue, X., Zaehle, S., 2020. Global carbon budget 2020. Earth Syst. Sci. Data 12, 3269–3340. https://doi.org/10.5194/ESSD-12-3269-2020.
Gaubert, B., Worden, H.M., Arellano, A.F.J., Emmons, L.K., Tilmes, S., Barré, J., Alonso, S.M., Vitt, F., Anderson, J.L., Alkemade, F., Houweling, S., Edwards, D.P., 2017. Chemical feedback from decreasing carbon monoxide emissions. Geophys. Res. Lett. 44, 9985–9995. https://doi.org/10.1002/2017GL074987.
Gisi, M., Hase, F., Dohe, S., Blumenstock, T., Simon, A., Keens, A., 2012. XCO_2-measurements with a tabletop FTS using solar absorption spectroscopy. Atmos. Meas. Tech. 5, 2969–2980. https://doi.org/10.5194/AMT-5-2969-2012.
Gruber, N., Bakker, D.C.E., DeVries, T., Gregor, L., Hauck, J., Landschützer, P., McKinley, G.A., Müller, J.D., 2023. Trends and variability in the ocean carbon sink. Nat. Rev. Earth Environ. 4, 119–134. https://doi.org/10.1038/S43017-022-00381-X.
Gulev, S.K., Thorne, P.W., Ahn, J., Dentener, F.J., Domingues, C.M., Gerland, S., Gong, D., Kaufman, D.S., Nnamchi, H.C., Quaas, J., 2021. Changing state of the climate system. In: Masson-Delmotte, V., Zhai, P., Pirani, A., Connors, S.L., Péan, S., Berger, S., Caud, N., Chen, Y., Goldfarb, L., Gomis, M.I. (Eds.), Climate Change 2021: the Physical Science Basis. Cambridge University Press, Cambridge, UK, pp. 287–422. https://doi.org/10.1017/9781009157896.004.
Hase, F., Frey, M., Kiel, M., Blumenstock, T., Harig, R., Keens, A., Orphal, J., 2016. Addition of a channel for XCO observations to a portable FTIR spectrometer for greenhouse gas measurements. Atmos. Meas. Tech. 9, 2303–2313. https://doi.org/10.5194/AMT-9-2303-2016.
Herkommer, B., Alberti, C., Castracane, P., Chen, J., Dehn, A., Dietrich, F., Deutscher, N. M., Frey, M.M., Groß, J., Gillespie, L., Hase, F., Morino, I., Pak, N.M., Walker, B., Wunch, D., 2024. Using a portable FTIR spectrometer to evaluate the consistency of Total Carbon Column Observing Network (TCCON) measurements on a global scale: The Collaborative Carbon Column Observing Network (COCCON) travel standard. Atmos. Meas. Tech. 17, 3467–3494. https://doi.org/10.5194/amt-17-3467-2024.
Hersbach, H., Bell, B., Berrisford, P., Hirahara, S., Horányi, A., Muñoz Sabater, J., Nicolas, J., Peubey, C., Radu, R., Schepers, D., Simmons, A., Soci, C., Dee, D., Thépaut, J.-N., et al., 2020. The ERA5 global reanalysis. Q. J. R. Meteorol. Soc. 146, 1999–2049. https://doi.org/10.1002/qj.3803.
Humpage, N., Boesch, H., Okello, W., Chen, J., Dietrich, F., Lunt, M.F., Feng, L., Palmer, P.I., Hase, F., 2024. Greenhouse gas column observations from a portable spectrometer in Uganda. Atmos. Meas. Tech. 17, 5679–5707. https://doi.org/10.5194/amt-17-5679-2024.
Jacob, D.J., 1999. Introduction to Atmospheric Chemistry. Princeton University Press, Princeton, NJ, USA.
Jacob, D.J., Varon, D.J., Cusworth, D.H., Dennison, P.E., Frankenberg, C., Gautam, R., Guanter, L., Kelley, J., McKeever, J., Ott, L.E., Poulter, B., Qu, Z., Thorpe, A.K., Worden, J.R., Duren, R.M., 2022. Quantifying methane emissions from the global scale down to point sources using satellite observations of atmospheric methane. Atmos. Chem. Phys. 22, 9617–9646. https://doi.org/10.5194/ACP-22-9617-2022.
Jain, P., Sharma, A.R., Acuna, D.C., Abatzoglou, J.T., Flannigan, M., 2024. Record-breaking fire weather in North America in 2021 was initiated by the Pacific Northwest heat dome. Commun. Earth Environ. 5, 202. https://doi.org/10.1038/s43247-024-01346-2.
Jiang, Z., Worden, J.R., Worden, H., Deeter, M., Jones, D.B.A., Arellano, A.F., Henze, D. K., 2017. A 15-year record of CO emissions constrained by MOPITT CO observations. Atmos. Chem. Phys. 17, 4565–4583. https://doi.org/10.5194/ACP-17-4565-2017.
Keenan, T.F., Williams, C.A., 2018. The terrestrial carbon sink. Annu. Rev. Environ. Resour. 43, 219–243. https://doi.org/10.1146/ANNUREV-ENVIRON-102017-030204.
Koukouli, M.E., Pseftogkas, A., Karagkiozidis, D., Mermigkas, M., Panou, T., Balis, D., Bais, A., 2025. Extreme wildfires over Northern Greece during summer 2023 – part B. Adverse effects on regional air quality. Atmos. Res. 320, 108034. https://doi.org/10.1016/J.ATMOSRES.2025.108034.
Lan, X., Tans, P., Thoning, K.W., 2025a. Trends in Globally-Averaged CO_2 Determined from NOAA Global Monitoring Laboratory Measurements. https://doi.org/10.15138/9N0H-ZH07.
Lan, X., Thoning, K.W., Dlugokencky, E.J., 2025b. Trends in globally-averaged CH_4, N_2O, and SF_6 determined from NOAA Global Monitoring Laboratory Measurements. https://doi.org/10.15138/P8XG-AA10.
Lelieveld, J., Gromov, S., Pozzer, A., Taraborrelli, D., 2016. Global tropospheric hydroxyl distribution, budget and reactivity. Atmos. Chem. Phys. 16, 12477–12493. https://doi.org/10.5194/acp-16-12477-2016.
MacDonald, C.G., Mastrogiacomo, J.P., Laughner, J.L., Hedelius, J.K., Nassar, R., Wunch, D., 2023. Estimating enhancement ratios of nitrogen dioxide, carbon monoxide and carbon dioxide using satellite observations. Atmos. Chem. Phys. 23, 3493–3516. https://doi.org/10.5194/ACP-23-3493-2023.
Makarova, M.V., Alberti, C., Ionov, D.V., Hase, F., Foka, S.C., Blumenstock, T., Warneke, T., Virolainen, Y.A., Kostsov, V.S., Frey, M., Poberovskii, A.V., Timofeyev, Y.M., Paramonova, N.N., Volkova, K.A., Zaitsev, N.A., Biryukov, E.Y., Osipov, S.I., Makarov, B.K., Polyakov, A.V., Ivakhov, V.M., Imhasin, H.Kh, Mikhailov, E.F., 2021. Emission Monitoring Mobile Experiment (EMME): an overview and first results of the St. Petersburg megacity campaign 2019. Atmos. Meas. Tech. 14, 1047–1073. https://doi.org/10.5194/amt-14-1047-2021.
Masoom, A., Fountoulakis, I., Kazadzis, S., Raptis, I.-P., Kampouri, A., Psiloglou, B.E., Kouklaki, D., Papachristopoulou, K., Marinou, E., Solomos, S., et al., 2023. Investigation of the effects of the Greek extreme wildfires of August 2021 on air quality and spectral solar irradiance. Atmos. Chem. Phys. 23, 8487–8514. https://doi.org/10.5194/acp-23-8487-2023.
Mermigkas, M., Topaloglou, C., Balis, D., Hase, F., Dubravica, D., 2025. Local and regional enhancements of GHGs in thessaloniki, inferred from ground-based FTIR measurements. Atmos. Res. 319, 108035. https://doi.org/10.1016/J.ATMOSRES.2025.108035.
Mermigkas, M., Topaloglou, C., Balis, D., Koukouli, M.E., Hase, F., Dubravica, D., Borsdorff, T., Lorente, A., 2021. FTIR measurements of greenhouse gases over thessaloniki, Greece in the framework of COCCON and comparison with S5P/TROPOMI observations. Remote Sens. 13. https://doi.org/10.3390/RS13173395. Page 3395 13.
Michailidis, K., Garane, K., Karagkiozidis, D., Peletidou, G., Voudouri, K.-A., Balis, D., Bais, A., 2024. Extreme wildfires over northern Greece during summer 2023 – part A: effects on aerosol optical properties and solar UV radiation. Atmos. Res. 311, 107700. https://doi.org/10.1016/j.atmosres.2024.107700.
Myhre, G., Shindell, D., Bréon, F.-M., Collins, W., Fuglestvedt, J., Huang, J., Koch, D., Lamarque, J.-F., Lee, D., Mendoza, B., Nakajima, T., Nakajima, T., Stephens, G., Takemura, T., Zhang, H., 2013. Anthropogenic and natural radiative forcing. In: Stocker, T.F., Qin, D., Plattner, G.-K., Tignor, M., Allen, S.K., Boschung, J., Nauels, A., Xia, Y., Bex, V., Midgley, P.M. (Eds.), Climate Change 2013: the Physical Science Basis. Contribution of Working Group I to the Fifth Assessment Report of the Intergovernmental Panel on Climate Change. Cambridge University Press, pp. 659–740. https://doi.org/10.1017/CBO9781107415324.018.
Pérez-Ramírez, D., Lyamani, H., Olmo, F., Whiteman, D., Alados-Arboledas, L., 2012. Columnar aerosol properties from sun-and-star photometry: statistical comparisons and day-to-night dynamic. Atmos. Chem. Phys. 12, 9719–9738. https://doi.org/10.5194/acp-12-9719-2012.

Radenz, M., Seifert, P., Baars, H., Floutsi, A.A., Yin, Z., Bühl, J., 2021. Automated time–height-resolved air mass source attribution for profiling remote sensing applications. Atmos. Chem. Phys. 21, 3015–3033. https://doi.org/10.5194/acp-21-3015-2021.

Rizos, K., Meleti, C., Kouvarakis, G., Mihalopoulos, N., Melas, D., 2022. Determination of the background pollution in the Eastern Mediterranean applying a statistical clustering technique. Atmos. Environ. 276, 119067. https://doi.org/10.1016/j.atmosenv.2022.119067.

Sedano, F., San-Miguel-Ayanz, J., Broglia, M., Durrant, T., Boca, R., Maianti, P., Jacome Felix Oom, D., Branco, A., De Rigo, D., Suarez-Moreno, M., Ferrari, D., Roglia, E., Scionti, N., Liberta', G., Tistan, A., 2025. Forest fires in Europe, Middle East and North Africa 2024. https://doi.org/10.2760/0649290.

Seibert, P., Beyrich, F., Gryning, S.-E., Joffre, S., Rasmussen, A., Tercier, P., 2000. Review and intercomparison of operational methods for the determination of the mixing height. Atmos. Environ. 34, 1001–1027. https://doi.org/10.1016/S1352-2310(99)00349-0.

Seinfeld, J.H., Pandis, S.N., 2016. Atmospheric Chemistry and Physics: from Air Pollution to Climate Change. John Wiley & Sons.

Sepúlveda, E., Schneider, M., Hase, F., Barthlott, S., Dubravica, D., García, O., Gomez-Pelaez, A., González, Y., Guerra, J., Gisi, M., et al., 2014. Tropospheric CH_4 signals as observed by NDACC FTIR at globally distributed sites and comparison to GAW surface in situ measurements. Atmos. Meas. Tech. 7, 2337–2360. https://doi.org/10.5194/amt-7-2337-2014.

Sha, M.K., Das, S., Frey, M.M., Dubravica, D., Alberti, C., Baier, B.C., Balis, D., Bezanilla, A., Blumenstock, T., Boesch, H., Cai, Z., Chen, J., Dandocsi, A., Mazière, M.D., Foka, S., García, O., Gillespie, L.D., Gribanov, K., Gross, J., Grutter, M., Handley, P., Hase, F., Heikkinen, P., Humpage, N., Jacobs, N., Jeong, S., Karppinen, T., Kiel, M., Kivi, R., Langerock, B., Laughner, J., Lopez, M., Makarova, M., Mermigkas, M., Morino, I., Mostafavipak, N., Nemuc, A., Newberger, T., Ohyama, H., Okello, W., Osterman, G., Park, H., Pirloaga, R., Pollard, D.F., Raffalski, U., Ramonet, M., Sepúlveda, E., Simpson, W.R., Stremme, W., Sweeney, C., Taquet, N., Topaloglou, C., Tu, Q., Warneke, T., Wunch, D., Zakharov, V., Zhou, M., 2025. Fiducial reference measurements for greenhouse gases (FRM4GHG): validation of satellite (Sentinel-5 Precursor, OCO-2, and GOSAT) missions using the COllaborative Carbon Column Observing Network (COCCON). Remote Sens. 17. https://doi.org/10.3390/rs17050734.

Sha, M.K., De Mazière, M., Notholt, J., Blumenstock, T., Chen, H., Dehn, A., Griffith, D. W.T., Hase, F., Heikkinen, P., Hermans, C., Hoffmann, A., Huebner, M., Jones, N., Kivi, R., Langerock, B., Petri, C., Scolas, F., Tu, Q., Weidmann, D., 2020. Intercomparison of low- and high-resolution infrared spectrometers for ground-based solar remote sensing measurements of total column concentrations of CO_2, CH_4, and CO. Atmos. Meas. Tech. 13, 4791–4839. https://doi.org/10.5194/amt-13-4791-2020.

Silva, S.J., Arellano, A.F., Worden, H.M., 2013. Toward anthropogenic combustion emission constraints from space-based analysis of urban CO_2/CO sensitivity. Geophys. Res. Lett. 40, 4971–4976. https://doi.org/10.1002/GRL.50954.

Stein, A.F., Draxler, R.R., Rolph, G.D., Stunder, B.J.B., Cohen, M.D., Ngan, F., 2015. NOAA's HYSPLIT atmospheric transport and dispersion modeling system. Bull. Am. Meteorol. Soc. 96, 2059–2077. https://doi.org/10.1175/BAMS-D-14-00110.1.

Stohl, A., 1998. Computation, accuracy and applications of trajectories—A review and bibliography. Atmos. Environ. 32, 947–966. https://doi.org/10.1016/S1352-2310(97)00457-3.

Stull, R.B., 1988. Mean boundary layer characteristics. In: An Introduction to Boundary Layer Meteorology. Springer, pp. 1–27. https://doi.org/10.1007/978-94-009-3027-8_1.

Szopa, S., Naik, V., Adhikary, B., Artaxo, P., Berntsen, T., Collins, W., Fuzzi, S., Gallardo, L., Kiendler-Scharr, A., Klimont, Z., Liao, H., Unger, N., Zanis, P., 2021. Short-lived climate forcers. In: Masson-Delmotte, V., Zhai, P., Pirani, A., Connors, S. L., Péan, C., Berger, S., Caud, N., Chen, Y., Goldfarb, L., Gomis, M.I., Huang, M., Leitzell, K., Lonnoy, E., Matthews, J.B.R., Maycock, T.K., Waterfield, T., Yelekçi, O., Yu, R., Zhou, B. (Eds.), Climate Change 2021: the Physical Science Basis. Contribution of Working Group I to the Sixth Assessment Report of the Intergovernmental Panel on Climate Change. Cambridge University Press, Cambridge, United Kingdom and New York, NY, USA, pp. 817–922. https://doi.org/10.1017/9781009157896.008.

Toledano, C., Cachorro, V., De Frutos, A., Torres, B., Berjon, A., Sorribas, M., Stone, R., 2009. Airmass classification and analysis of aerosol types at El Arenosillo (Spain). J. Appl. Meteorol. Climatol. 48 (1), 962–981. https://doi.org/10.1175/2008JAMC2006.

Tu, Q., Hase, F., Schneider, M., García, O., Blumenstock, T., Borsdorff, T., Frey, M., Khosrawi, F., Lorente, A., Alberti, C., Bustos, J.J., Butz, A., Carreño, V., Cuevas, E., Curcoll, R., Diekmann, C.J., Dubravica, D., Ertl, B., Estruch, C., León-Luis, S.F., Marrero, C., Morgui, J.-A., Ramos, R., Scharun, C., Schneider, C., Sepúlveda, E., Toledano, C., Torres, C., 2022. Quantification of CH_4 emissions from waste disposal sites near the city of Madrid using ground- and space-based observations of COCCON, IASI. Atmos. Chem. Phys. 22, 295–317. https://doi.org/10.5194/acp-22-295-2022.

Vogel, F.R., Frey, M., Staufer, J., Hase, F., Broquet, G., Xueref-Remy, I., Chevallier, F., Ciais, P., Sha, M.K., Chelin, P., Jeseck, P., Janssen, C., Té, Y., Groß, J., Blumenstock, T., Tu, Q., Orphal, J., 2019. XCO_2 in an emission hot-spot region: the COCCON Paris campaign 2015. Atmos. Chem. Phys. 19, 3271–3285. https://doi.org/10.5194/acp-19-3271-2019.

Wuebbles, D.J., Hayhoe, K., 2002. Atmospheric methane and global change. Earth Sci. Rev. 57, 177–210. https://doi.org/10.1016/S0012-8252(01)00062-9.

Wunch, D., Toon, G.C., Blavier, J.F.L., Washenfelder, R.A., Notholt, J., Connor, B.J., Griffith, D.W.T., Sherlock, V., Wennberg, P.O., 2011. The Total Carbon Column Observing Network. Philos. Trans. R. Soc. A Math. Phys. Eng. Sci. 369, 2087–2112. https://doi.org/10.1098/RSTA.2010.0240.

Zheng, B., Chevallier, F., Yin, Y., Ciais, P., Fortems-Cheiney, A., Deeter, M.N., Parker, R. J., Wang, Y., Worden, H.M., Zhao, Y., 2019. Global atmospheric carbon monoxide budget 2000-2017 inferred from multi-species atmospheric inversions. Earth Syst. Sci. Data 11, 1411–1436. https://doi.org/10.5194/ESSD-11-1411-2019.

Zhong, Q., Huang, Y., Shen, H., Chen, Y., Chen, H., Huang, T., Zeng, E.Y., Tao, S., 2017. Global estimates of carbon monoxide emissions from 1960 to 2013. Environ. Sci. Pollut. Res. 24, 864–873. https://doi.org/10.1007/S11356-016-7896-2.